TECHNISCHE UNIVERSITÄT WIEN

Thermal Modelling of Revolving Steel Belts

Diplomarbeit

Richard Schreiner

TECHNISCHE
UNIVERSITÄT
WIEN

DIPLOMARBEIT

Thermal Modelling of Revolving Steel Belts

ausgeführt zum Zwecke der Erlangung
des akademischen Grades eines Diplom-Ingenieurs
unter der Leitung von

Assistant Prof. Dipl.-Ing. Dr.techn. Florian Toth
Mitwirkung Vladimir Filkin, MSc
Institut für Mechanik und Mechatronik, E325 A4

eingereicht an der Technischen Universität Wien
Fakultät für Maschinenwesen und Betriebswissenschaften
von

Richard Schreiner, BSc
Wien, am 10.03.2025 Unterschrift

Eidesstattliche Erklärung

Ich habe zur Kenntnis genommen, dass ich zur Drucklegung meiner Arbeit unter der Bezeichnung

DIPLOMARBEIT

nur mit Bewilligung der Prüfungskommission berechtigt bin.

Ich erkläre an Eides statt, dass die vorliegende Arbeit nach den anerkannten Grundsätzen für wissenschaftliche Abhandlungen von mir selbstständig erstellt wurde.

Alle verwendeten Hilfsmittel, insbesondere die zugrunde gelegte Literatur, sind in dieser Arbeit genannt und aufgelistet. Die aus den Quellen wörtlich entnommenen Stellen sind als solche kenntlich gemacht.

Das Thema dieser Arbeit wurde von mir bisher weder im In- noch Ausland einer Beurteilerin/einem Beurteiler zur Begutachtung in irgendeiner Form als Prüfungsarbeit vorgelegt. Diese Arbeit stimmt mit der von den Begutachterinnen/Begutachtern beurteilten Arbeit überein. Ich nehme zur Kenntnis, dass die vorgelegte Arbeit mit geeigneten und dem derzeitigen Stand der Technik entsprechenden Mittel (Plagiat-Erkennungssoftware) elektronisch-technisch überprüft wird. Dies stellt einerseits sicher, dass bei der Erstellung der vorgelegten Arbeit die hohen Qualitätsvorgaben im Rahmen der geltenden Regeln zur Sicherung guter wissenschaftlicher Praxis an der TU Wien eingehalten wurden. Zum anderen werden durch einen Abgleich mit anderen studentischen Abschlussarbeiten Verletzungen meines persönlichen Urheberrechts vermieden.

Wien, am 10.03.2025 Unterschrift

Danksagung

Zunächst möchte ich mich herzlich bei meinen Betreuern, Herrn Prof. Dr. Florian Toth und Herrn Vladimir Filkin, für die Unterstützung bei der Erstellung dieser Arbeit bedanken. Sie standen mir stets mit Rat und Tat zur Seite und ermöglichten es mir, meinen Interessen weitgehend freien Lauf zu lassen.

Nun ist diese Arbeit der abschließende Teil meines Studiums, und damit geht für mich auch ein besonderer Lebensabschnitt zu Ende, in dem ich nicht nur vieles Lernen, sondern auch so manche Herausforderung meistern durfte.

Ganz wie der Zieleinlauf eines Marathons, so scheint der Abschluss eines Studiums zunächst wie eine Einzelleistung. Doch beides erfordert ein zuverlässiges Team, das unterstützt und motiviert, damit man die lange Zeit der Vorbereitung und auch die letzten Meter gut meistern kann.

Deswegen möchte ich mich hier bei meinem persönlichen Team bedanken: bei all meinen Freunden und meiner Familie, und ganz besonders bei meiner Frau Alexandra, die mir auch in den schwierigsten Phasen ein Leuchtturm war, der mir Hoffnung und Zuversicht gespendet hat.

Ohne euch hätte ich das nicht geschafft.

Contents

Abstract

This thesis investigates the thermal behavior of revolving steel belts, with a special emphasis on induction heating. These systems play a critical role in industrial applications such as food processing, chemical manufacturing, or paper production.

To analyze the thermal effects, numerical simulations based on the finite element method (FEM) are employed. The primary challenge lies in efficiently modeling the coupled interaction of electromagnetic, mechanical, and thermal fields to predict temperature distributions and deformation patterns. The focus of this work lies in the investigation of the influence of a belt's motion and deformation on the temperature field.

By solving Laplace's equation for the velocity potential, a correction approach is used to refine velocity fields in deformed sheets. Additionally, a practical error estimation method is proposed to predict average temperature errors without the need for explicit solutions of the corrected and uncorrected problem.

A parameter study on a two-dimensional (2D) model quantifies the influence of deformation and speed on temperature errors, with findings validated through a fully coupled three-dimensional (3D) simulation incorporating electromagnetic heating, mechanical deformation, and thermal conduction. The results demonstrate the impact of velocity corrections on thermal accuracy.

Kurzfassung

In dieser Arbeit wird das thermische Verhalten von umlaufenden Stahlbändern untersucht, wobei ein besonderer Schwerpunkt auf der Induktionserwärmung liegt. Diese Systeme spielen eine entscheidende Rolle in industriellen Anwendungen wie der Lebensmittelverarbeitung, der chemischen Produktion oder der Papierherstellung.

Zur Analyse des thermischen Verhaltens werden numerische Simulationen auf der Grundlage der Finite-Elemente-Methode (FEM) durchgeführt. Die größte Herausforderung besteht darin, die gekoppelte Interaktion von elektromagnetischen, mechanischen und thermischen Feldern effizient zu modellieren, um Temperaturverteilungen und Verformungsmuster vorherzusagen. Der Schwerpunkt dieser Arbeit liegt auf der Untersuchung der Wechselwirkung zwischen der Bewegung und Verformung des Bandes und dem Temperaturfeld.

Durch die Lösung der Laplace-Gleichung für das Geschwindigkeitspotenzial wird ein Korrekturansatz zur Verfeinerung der Geschwindigkeitsfelder in deformierten Blechen verwendet. Darüber hinaus wird eine praktische Methode zur Fehlerabschätzung vorgeschlagen, um durchschnittliche Temperaturfehler vorherzusagen, ohne dass explizite Lösungen des korrigierten und unkorrigierten Problems erforderlich sind.

Eine Parameterstudie an einem zweidimensionalen (2D) Modell quantifiziert den Einfluss von Verformung und Geschwindigkeit auf Temperaturfehler, wobei die Ergebnisse durch eine vollständig gekoppelte dreidimensionale (3D) Simulation unter Einbeziehung von elektromagnetischer Erwärmung, mechanischer Verformung und Wärmeleitung validiert werden. Die Ergebnisse zeigen den Einfluss von Geschwindigkeitskorrekturen auf das Temperaturfeld.

Notation

Symbols

a	m	Inductor coil leg/beam width
α	$\mathrm{W\,m^{-2}\,K^{-1}}$	Heat transfer coefficient
b	m	Belt/sheet width
C		Tuning/weighting parameter
C_J		Joule loss width factor
C_tb		Top and bottom curve of slice
c	$\mathrm{m^{-1}}$	Exponential factor
c_p	$\mathrm{J\,m^{-3}\,K^{-1}}$	Isobaric heat capacity
ΔT	K	Velocity-related temperature error
$\Delta\bar{T}$	K	Velocity-related temperature (averaged over cross-section)
$\Delta T_\mathrm{c,tb}$	K	Top-bottom temperature difference (corrected case)
$\Delta T_\mathrm{u,tb}$	K	Top-bottom temperature difference (uncorrected case)
$\Delta\tilde{T}_\mathrm{tb}$	K	Approximation of ΔT_tb
$\Delta T_\mathrm{top/bot}$	K	Temperature error on top or bottom surface/curve
$\Delta\bar{T}_\mathrm{out}$	K	Temperature error averaged over outflow boundary
Δx	m	Distance, error section length
Δx_m	m	Length of m-th error section
E	J	Energy
f_u		Error forcing
$F_{\mathrm{u},m}$	$\mathrm{K\,m^{-1}}$	Section error contribution
h	m	Belt/sheet thickness
k	$\mathrm{W\,m^{-1}\,K^{-1}}$	Thermal conductivity
κ	$\mathrm{m^2\,s^{-1}}$	Diffusion coefficient
L	m	Domain or sheet length
L_B	m	Belt length
L_D	m	Characteristic diffusion length
Ψ		Velocity potential
ρ	$\mathrm{kg/m^3}$	Density
Pe		Peclet number
$\dot{Q}$	W	Heat flux
$\dot{q}$	$\mathrm{W/m^3}$	Power density
$\dot{q}_\mathrm{J}$	$\mathrm{W/m^3}$	Joule losses
St		Stanton number
t	s	Time
T	K	Temperature
T_∞	K	Ambient temperature
T_c	K	Corrected temperature
T_u	K	Uncorrected temperature
T_in	K	Inflow temperature
T_out	K	Outflow temperature
Θ_m		Step function for error section
$\tilde{x}$		Normalized coordinate
U	J	Internal energy
v_0	m/s	Belt speed
w	m	Displacement in z-direction
$w' := \frac{dw}{dx}$		Displacement derivative

x	m	Cartesian coordinate
y_{s}	m	Position of cross-section/slice
Ω		Domain
$\partial\Omega$		Domain boundary
Ω_{B}		Belt domain
Ω_{s}		Sheet domain
Ω_{s}^{+}		Adjacent sheet domain (downstream)
Ω_{s}^{-}		Adjacent sheet domain (upstream)
$\partial\Omega$		Domain boundary
Γ_{bot}		Bottom boundary
Γ_{in}		Inflow boundary
Γ_{out}		Outflow boundary
Γ_{top}		Top boundary
$\boldsymbol{C}$	Pa	Stiffness tensor
$\boldsymbol{f}$	$\mathrm{N\,m^{-3}}$	Force density
$\boldsymbol{q}$	$\mathrm{W\,m^{-2}}$	Heat flux density
$\boldsymbol{t}$	$\mathrm{N\,m^{-2}}$	Traction forces
$\boldsymbol{v}$	m/s	Velocity
$\boldsymbol{v}_{\mathrm{u}}$	m/s	Uncorrected velocity
$\boldsymbol{v}_{\mathrm{c}}$	m/s	Corrected velocity
$\boldsymbol{x}$	m	Coordinate vector
$\boldsymbol{e}$		Unit vector
$\boldsymbol{n}$		Normal vector

Operators

$\partial_{x_{\mathrm{i}}}(\cdot)$	Partial derivative
$\frac{d}{dx}(\cdot) = (\cdot)'$	Spatial derivative
$\lvert\cdot\rvert$	Absolute value
$\max_x(\cdot)$	Maximum operator w.r.t x variable
$\hat{(\cdot)}$	(Estimated) peak value
∇	Gradient
$\overline{(\cdot)}$	Spatial (surface/curve) average

Acronyms

CFD	Computational Fluid Mechanics
FE/FEM	Finite Element (Method)
FSI	Fluid Structure Interaction
FVM	Finite Volume Method
PDE	Partial Differential Equation

1 Introduction

Due to their versatility, industrial steel belt systems find applications in a variety of industries. In many processes, for example in paper- or food production, it is crucial to not only transport material, but to also tightly control heat and temperature along the belt. A particularly interesting solution, is to directly heat a steel belt via induction heating, see Figure 1.1.

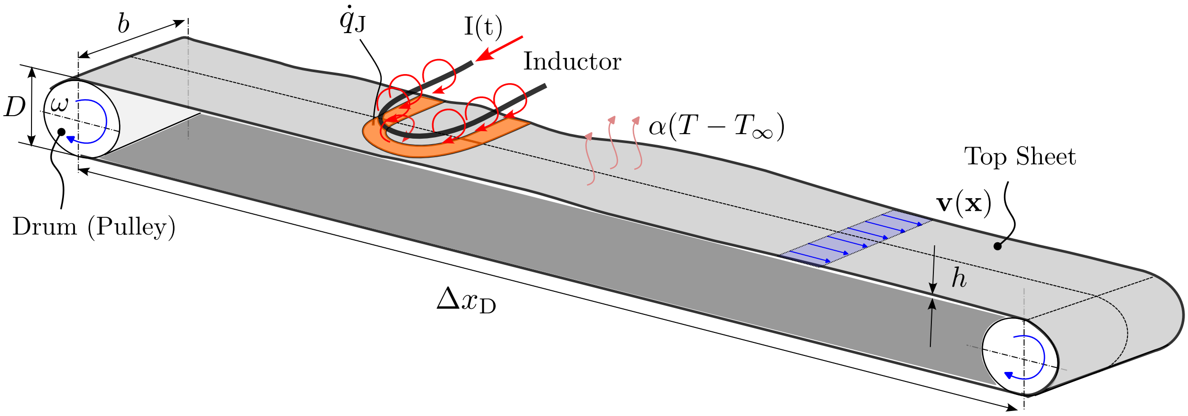

Figure 1.1: Overview of a steel belt with induction heating. The belt with velocity $\boldsymbol{v}(\boldsymbol{x})$ is driven by a drum rotating with angular velocity ω. The most important dimensions are width b, thickness h, drum (or pulley) distance Δx_D and diameter D.

In inductive belt heating, an inductor is driven by an alternating current to create a magnetic field. This induces eddy currents in the sheet which are dissipated as Joule losses that heat up the belt sheet. Inductive heating has some advantages over conventional methods such as hot-air fans. For one, higher efficiencies may be reached, and no direct contact is needed. Also, high energy densities make it possible to quickly heat up material. However, this poses some challenges too: due to these drastic temperature gradients, significant deformations and even buckling phenomena may occur. Such downsides can be mitigated by providing the design engineers with precise, efficient and practical simulation methods.

To simulate a belt, the problem is modelled mathematically using coupled partial differential equations (PDEs). This mathematical model of the system must be solved numerically. In the context of inductive belt heating, three primary physical fields are involved: the electromagnetic (EM) field, the mechanical field, and the thermal (temperature) field. The finite-element method (FEM) is a widely used technique for simulating such coupled multi-physics problems [5].

This work builds on previous contributions [7, 3], and investigates an improved method to simulate the thermal field for deforming belts.

For this, the following approach to model a belt with induction heating is used, see Figure 1.2 and Figure 1.3:

- **Mechanical Problem**: The belt's top sheet, is modelled using shell elements [12] and is assumed to be quasi-static.

- **Electromagnetic (EM) Problem**: To avoid an expensive transient simulation of the EM field, a method that leverages the faster dynamics of the EM problem compared to the thermal or mechanical problems is used [7, 8]. Detailed information can be found in the cited resources.
- **Thermal Problem**: The thermal problem is modelled using the steady-state heat conduction equation for a moving sheet. To capture temperature variations through the thickness, 3D elements are employed.
- **Coupling**: The temperature field is forward-coupled to the shell model. External loads and thermal expansion cause deformations in the shell model, which are then applied to the 3D grids of the EM and thermal problems by solving a grid smoothing problem. This work introduces and investigates an additional step to adapt the velocity field to the deformed geometry.

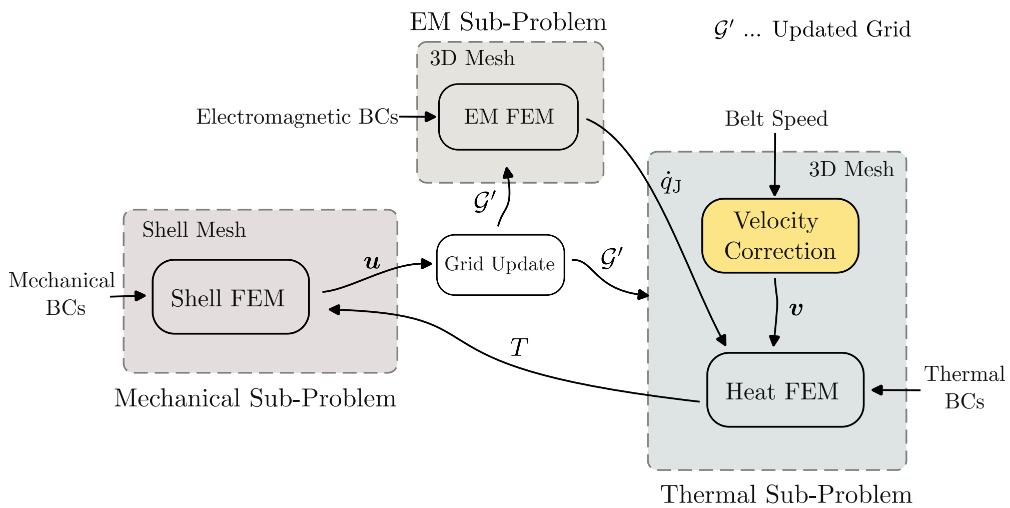

Figure 1.2: Overview of the coupling approach used in this work. The focus of this work lies in the thermal sub-problem. An additional step is introduced to correct the velocity field for deformation.

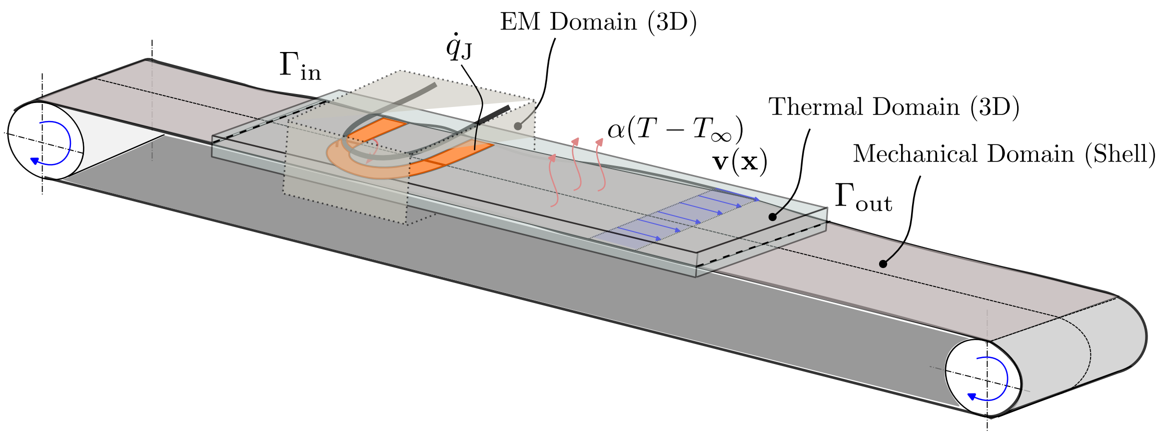

Figure 1.3: Sketch of a belt's top sheet model. The mechanical domain consists of shell elements. The thermal and EM domains are modelled using 3D elements, and share the same grid for the sheet.

Using this framework, this work aims to improve the accuracy of the thermal sub-problem by investigating an enhanced coupling between the mechanical and thermal sub-problems.

For a straight, undeformed sheet, the velocity is a simple unidirectional vector field. However, as the sheet deforms, the velocity field must be corrected accordingly. This correction involves solving a Laplace equation for the velocity potential. Neglecting this correction results in a spurious energy flux through the bounding surfaces of the belt's sheet, leading to a temperature error. However, this additional computational step increases the simulation cost, especially in a coupled, potentially non-linear problem, as it accumulates at every iteration. Depending on the magnitude of the temperature error, this cost may not always be justified. The goal of this work is to investigate the necessity and implications of the velocity correction on the temperature field.

After introducing the governing equations, the temperature fields for both constant velocity (uncorrected) and conforming velocity (corrected) cases are compared using energy balances. The discrepancy between these temperature fields is termed the *velocity-related temperature error*. An expression for the thickness-averaged velocity-related temperature error is derived, revealing that this error is significant only in regions with substantial through-the-thickness temperature variations. Based on this insight, a practical method is proposed to estimate the thickness-averaged velocity-related temperature error for specific sections of a belt sheet. This method utilizes peak temperature and deformation differences. These theoretical findings are then compared in a numerical experiment using a simple single-field 2D model. Finally, the methods are applied in a more realistic coupled magnetic-thermo-mechanical simulation of a sheet with induction heating.

2 Governing Equations

In this chapter, the governing equations for the thermal problem are presented.

First, the heat conduction PDE for a moving sheet is derived, resulting in a convection-diffusion equation with an additional velocity term. Since all involved PDEs in this work are solved using the finite element method, the process of discretizing the weak form using the Galerkin method is demonstrated.

In the second part of the chapter, the method for correcting the velocity field for a deformed sheet is presented. The assumptions lead to Laplace's equation, which is also briefly examined.

2.1 Heat Conduction

This section derives the heat conduction equation for a moving sheet. The classical heat conduction equation is derived from the first law of thermodynamics, which states the *conservation of energy* as

$$\frac{dU}{dt} = \dot{Q}(t) + P(t), \tag{2.1}$$

where U is the internal energy, $\dot{Q}$ is the heat supply, and P is the mechanical power. In this work, the mechanical power term is assumed to be negligible compared to the heat supply and can be omitted.

In a continuum formulation, these quantities relate to an infinitesimal material element $\rho d\Omega$. The internal energy is given by

$$U = \int_{\Omega} \rho u \, d\Omega, \tag{2.2}$$

where u is the *specific internal energy*.

The heat supply is expressed as

$$\dot{Q} = \int_{\Omega} \dot{q} \, d\Omega - \int_{\partial\Omega} \mathbf{q} \cdot \mathbf{n} \, d\Gamma, \tag{2.3}$$

where $\dot{q}$ represents a power density and $\mathbf{q}$ denotes heat fluxes on the domain interface.

Applying Reynolds' transport theorem to account for the belt's motion, the following equation is obtained

$$\frac{dU}{dt} = \frac{d}{dt} \int_{\Omega(t)} \rho c_{\mathrm{p}} T \, d\Omega = \int_{\Omega} \partial_t \rho c_{\mathrm{p}} T \, d\Omega + \int_{\partial\Omega} \rho c_{\mathrm{p}} T \mathbf{v} \cdot \mathbf{n} \, d\Gamma, \tag{2.4}$$

where $\mathbf{v}$ is the velocity of the domain.

This leads to the global heat balance for a moving body

$$\int_\Omega \partial_t \rho c_\mathrm{p} T \, d\Omega + \int_{\partial\Omega} \rho c_\mathrm{p} T \mathbf{v} \cdot \mathbf{n} \, d\Gamma = \int_\Omega \dot{q} \, d\Omega - \int_{\partial\Omega} \mathbf{q} \cdot \mathbf{n} \, d\Gamma. \tag{2.5}$$

Using the global heat balance, the convection-diffusion equation can now be derived.

2.1.1 The Convection-Diffusion Equation

With the help of the divergence theorem, the global heat balance (2.5) can be stated as

$$\int_\Omega (\partial_t \rho c_\mathrm{p} T + \nabla \cdot (\rho c_\mathrm{p} T \mathbf{v}) - \dot{q} + \nabla \cdot \mathbf{q}) d\Omega = 0, \tag{2.6}$$

which yields the *local heat balance*

$$\partial_t \rho c_\mathrm{p} T + \nabla \cdot (\rho c_\mathrm{p} T \mathbf{v}) = \dot{q} - \nabla \cdot \mathbf{q}. \tag{2.7}$$

The velocity term can be split into two contributions

$$\nabla \cdot (\rho c_\mathrm{p} T \mathbf{v}) = \rho c_\mathrm{p} (\mathbf{v} \cdot \nabla T) + \rho c_\mathrm{p} T (\nabla \cdot \mathbf{v}), \tag{2.8}$$

where for an incompressible body, the condition

$$\nabla \cdot \mathbf{v} = 0, \tag{2.9}$$

is fulfilled and only the following term remains

$$\nabla \cdot (\rho c_\mathrm{p} T \mathbf{v}) = \rho c_\mathrm{p} (\mathbf{v} \cdot \nabla T). \tag{2.10}$$

Inside the body the heat flux $\mathbf{q}$ is due to heat conduction, which is described by *Fourier's law*

$$\mathbf{q} = -k \nabla T, \tag{2.11}$$

where k is the *thermal conductivity*. For materials that show non-isotropic behavior, for example wood or graphite, k is a second-order tensor. In this work, only homogenous, isotropic materials, are considered, reducing k to a scalar. Moreover, as a simplification, k is set constant, and temperature dependence is neglected.

Now, by plugging (2.11) into (2.7), the convection-diffusion equation[1] can be found. This PDE describes the heat conduction problem inside an incompressible, moving material domain. For space and time-independent density and conductivity, it reads

$$\frac{\partial T}{\partial t} + \boldsymbol{v} \cdot \nabla T - \kappa \nabla^2 T = \frac{1}{\rho c} \dot{q}, \tag{2.12}$$

where the *thermal diffusivity* is defined as

$$\kappa = k/(\rho c). \tag{2.13}$$

The heat conduction inside the body is coupled to its surroundings via boundary conditions (BCs). There are three types considered[2] here:

[1] Also known as *advection-diffusion* equation.
[2] Radiative heat transfer will be neglected, as this is more relevant to very high temperature applications.

- Prescribed temperature T_e on Γ_{e} (Dirichlet BC)
- Prescribed heat flux q_{n} on Γ_{n} (Neumann BC)
- Heat transfer with a surrounding fluid on Γ_α. This is typically modelled as,

$$\boldsymbol{q} \cdot \boldsymbol{n} = \alpha(T - T_\infty), \tag{2.14}$$

where α is the heat transfer coefficient and T_∞ a reference temperature[3].

For this work, it was assumed that α is in the range of $1\,\mathrm{W/(m^2K)}$ to $100\,\mathrm{W/(m^2K)}$, which are realistic average values for a moving plate at the investigated speeds, without additional draft.

It is important to note that the processes on the fluid-solid interface can be very complex. A significant portion of the heat and mass transfer literature focuses on accurately calculating the heat transfer coefficient. For gaseous fluids, [10] provides a range of $2\,\mathrm{W/(m^2K)}$ to $25\,\mathrm{W/(m^2K)}$ for natural convection and up to $250\,\mathrm{W/(m^2K)}$ for forced convection. To accurately calculate the heat transfer coefficient for an industrial steel belt, the precise setup would need to be known. Even then, according to [1], an error of 25% is typical in engineering calculations of α. For example, a side draft from a fan or adjacent devices may significantly influence the local heat transfer coefficient. Additionally, the moving and possibly deforming belt may itself cause perturbations in the surrounding airflow, further complicating the heat transfer.

Apart from the boundary conditions, the induction heating itself can be captured using a volume coupling with the Joule losses, expressed as

$$\dot{q}_{\mathrm{J}} = \boldsymbol{J} \cdot \boldsymbol{E}, \tag{2.15}$$

where $\boldsymbol{J}$ is the electric current density and $\boldsymbol{E}$ the electric field intensity.

2.1.2 Classification and Fundamental Properties

To inspect some fundamental aspects of the convection-diffusion equation, it is useful to bring the equation into a *dimensionless form*, which can be obtained as

$$\frac{\partial \tilde{T}}{\partial \tilde{t}} + \tilde{\boldsymbol{v}} \cdot \tilde{\nabla} \tilde{T} - \mathrm{Pe}^{-1} \tilde{\nabla}^2 \tilde{T} = \tilde{\dot{q}}, \tag{2.16}$$

where the definition of the *Peclet number*

$$\mathrm{Pe} := \frac{vl}{\kappa}, \tag{2.17}$$

with characteristic length l and velocity v was introduced.

The Peclet number shows the relation between the convective and the diffusive term. The problem is said to be *convection dominant* if

$$\mathrm{Pe} \gg 1. \tag{2.18}$$

Likewise, *diffusion dominance* is observed if

$$\mathrm{Pe} \ll 1. \tag{2.19}$$

In a two- or three-dimensional problem, the Peclet number is typically direction-dependent. In the case of the axially moving sheet, it can be said that, in the direction of motion, the problem

[3] In a belt application this is typically the room or ambient temperature of the surrounding air.

becomes quickly convection-dominant, even at low speeds, and the first-order terms dominate. However, in the direction normal to the bulk motion, i.e., in the thickness direction, the diffusive term cannot be neglected.

In general, the stationary convection-diffusion equation presents a location-dependent mixture of *elliptic* and *hyperbolic* behavior, as shown in Table 2.1. More detailed treatments can be found in the extensive literature on this topic, for example [13, 14].

Time-dependence	$\mathrm{Pe} \ll 1$	$\mathrm{Pe} \gg 1$
Instationary	Parabolic	Hyperbolic
Stationary	Elliptic	Hyperbolic

Table 2.1: Dominant classification of the convection-diffusion equation.

2.1.3 Weak Form of the Steady-State Problem

To obtain the weak formulation from the strong formulation of a problem, a PDE is multiplied by a *test function*[4] T' and integrated over the domain. Using the steady-state convection-diffusion equation (2.12), again with general flux, this reads

$$\int_\Omega T'(\boldsymbol{v} \cdot \rho c_\mathrm{p} \nabla T + \nabla \cdot \boldsymbol{q} - \dot{q}) d\Omega = 0. \tag{2.20}$$

The next step towards a weak formulation is to incorporate the boundary conditions with the help of appropriate integral theorems.

For the second term in (2.20), this yields

$$\int_\Omega T'(\boldsymbol{v} \cdot \rho c_\mathrm{p} \nabla T) d\Omega = \rho c_\mathrm{p} \int_{\partial\Omega} T'(\boldsymbol{v}T \cdot \boldsymbol{n}) d\Gamma - \rho c_\mathrm{p} \int_\Omega \nabla T' \cdot (\boldsymbol{v}T) d\Omega, \tag{2.21}$$

where the divergence theorem (see e.g. Appendix in [5]) was used. The boundary integrals on $\partial\Omega$ can be further split over a finite set of non-overlapping subdomains. In practice, there may be many subdomains, reflecting a complicated set of boundary conditions. However, from a general point of view, there exist only two types:

- *Essential Boundary Conditions* on region Γ_e:

  Here, the primary unknown T is explicitly enforced. These are identically fulfilled via the use of an appropriate function space.

- *Natural Boundary Conditions* on region Γ_n:

  On these, a relation to a derivative of T is given – for example, a *flux*. This type of condition is enforced via the integrals in the weak form.

Thus, by splitting the boundary into an essential and natural part $\partial\Omega = \Gamma_\mathrm{n} \cup \Gamma_\mathrm{e}$, the following contribution of the second term in (2.20) remains:

$$\int_\Omega T'(\boldsymbol{v} \cdot \rho c_\mathrm{p} \nabla T) d\Omega = \rho c_\mathrm{p} \int_{\Gamma_\mathrm{n}} T'(\boldsymbol{v}T \cdot \boldsymbol{n}) d\Gamma - \rho c_\mathrm{p} \int_\Omega \nabla T' \cdot (\boldsymbol{v}T) d\Omega. \tag{2.22}$$

[4]The test function needs to satisfy the boundary conditions but is otherwise arbitrarily chosen.

Analogously, the flux term in (2.20) results in

$$\int_{\Omega} T'(\nabla \cdot \boldsymbol{q})d\Omega = \int_{\partial\Omega} T'(\boldsymbol{q} \cdot \boldsymbol{n})d\Gamma - \int_{\Omega} \nabla T' \cdot \boldsymbol{q}d\Omega. \tag{2.23}$$

Again, using Fourier's law (2.11) within the domain, yields

$$\int_{\Omega} \nabla T' \cdot \boldsymbol{q}d\Omega = -\int_{\Omega} \nabla T' \cdot k\nabla T d\Omega, \tag{2.24}$$

and for the boundary term, a heat transfer BC, can be incorporated as well

$$\int_{\partial\Omega} T'(\boldsymbol{q} \cdot \boldsymbol{n})d\Gamma = \int_{\Gamma_\alpha} T'\alpha(T - T_\infty)d\Gamma + \int_{\Gamma_\mathrm{n}} T' q_\mathrm{n} d\Gamma, \tag{2.25}$$

resulting in

$$\begin{aligned} \int_{\Omega} T'(\nabla \cdot \boldsymbol{q})d\Omega = &\int_{\Gamma_\alpha} T'\alpha(T - T_\infty)d\Gamma \\ &+ \int_{\Gamma_\mathrm{n}} T' q_\mathrm{n} d\Gamma + \int_{\Omega} \nabla T' \cdot k\nabla T d\Omega. \end{aligned} \tag{2.26}$$

Collecting (**??**) and (2.26) the weak form can be stated as:

Definition 1 (Weak Steady-State Convection-Diffusion Problem)**.** Given the incompressible velocity field

$$\boldsymbol{v}(\boldsymbol{x}) : \bar{\Omega} \to \bar{\Omega}. \tag{2.27}$$

Find the temperature field $T(\boldsymbol{x})$, such that for all test functions T' the equation

$$\begin{aligned} \rho c_\mathrm{p} \int_{\Omega} \nabla T' \cdot [k/(\rho c_\mathrm{p})\nabla T - \boldsymbol{v}T]d\Omega + \rho c_\mathrm{p} \int_{\Gamma_\mathrm{n}} T'(\boldsymbol{v}T \cdot \boldsymbol{n})d\Gamma \\ + \int_{\Gamma_\alpha} T'\alpha(T - T_\infty)d\Gamma = \int_{\Omega} T'\dot{q}d\Omega - \int_{\Gamma_q} T' q_\mathrm{n} d\Gamma \end{aligned} \tag{2.28}$$

is satisfied.

2.1.4 Galerkin Discretization

Both, the weak and strong formulation, are *infinite-dimensional* problems. To arrive at a *finite-dimensional* approximation, the following ansatz is made

$$T^h = T_e + \sum_{a=1}^{n_{eq}} N_a(\boldsymbol{x})T_a(t) \approx T, \tag{2.29}$$

where T_e is a function satisfying the essential boundary condition on Γ_e, h is a discretization parameter, N_a are *shape functions*[5], which are scaled by n_{eq} unknown coefficients T_a. Moreover, the function T_e too, is approximated as

$$T_e = \sum_{b=1}^{n_e} N_b(\boldsymbol{x})T_{eb}(t), \tag{2.30}$$

[5] Also known as *basis* or *interpolation* functions.

with n_e *known* coefficients T_{eb} and shape functions N_b.

Also, a finite approximation of the test function $T'^h \approx T'$ has to be defined. In the classical *Galerkin* method the same ansatz as for the primary unknown T is used. However, doing so is not strictly necessary and other variants exist. These are referred to as *Petrov-Galerkin methods* [4]. Because the classical Galerkin method can lead to instabilities in convection-diffusion problems, alternatives within the Petrov-Galerkin framework have been established [2, 14]. Because in this work no stability issues were encountered, these methods are not further discussed here.

Now, to obtain a system of equations, both T^h and T'^h are plugged into the weak formulation. Because this equation has to hold for any test function, n_{eq} linear-independent equations can be found. Switching to matrix notation for the unknowns T_i,

$$\underline{T} = [T_1, T_2, \cdots, T_i, \cdots, T_{eq}]^T, \tag{2.31}$$

the following linear system can be found

$$\boldsymbol{K}\underline{T} = \boldsymbol{f}, \tag{2.32}$$

with *thermal stiffness matrix* $\boldsymbol{K}$ and *forcing vector* $\boldsymbol{f}$.

These *global* system matrices/vectors are constructed from the following entries

$$\boldsymbol{K} = [K]_{ij} = \int_\Omega \nabla N_i \cdot \boldsymbol{v} N_j \rho c_\mathrm{p} + \nabla N_i \cdot k \cdot \nabla N_j d\Omega + \int_{\Gamma_\alpha} N_i N_j \alpha d\Gamma \tag{2.33}$$

$$\begin{aligned}\boldsymbol{f} = [f]_i = &\int_\Omega N_i \dot{q} d\Omega - \int_{\Gamma_q} N_i q_\mathrm{n} d\Gamma + \int_{\Gamma_\alpha} \alpha T_\infty d\Gamma \\ &- \sum_{b=1}^{n_e} \{ \int_\Omega \nabla N_i \cdot k \cdot \nabla N_b - \nabla N_i \cdot \boldsymbol{v} N_b (\rho c_\mathrm{p}) d\Omega \, T_{eb} \},\end{aligned} \tag{2.34}$$

which can be constructed in a procedural manner from the local contributions of *finite elements*. For a detailed treatment, refer to rich literature on the FEM, e.g., [5, 4, 15].

2.2 Velocity Correction and Laplace's Equation

In the preceding sections it was shown how the heat conduction problem for a moving body can be formulated in a space-fixed, or *Eulerian*, reference system. Then, the belt's motion is captured via an additional velocity term. The question remains how the velocity term for a deformed sheet can be calculated. In the case that a sheet is perfectly straight, i.e., with zero curvature, it can be assumed that the velocity is uniform and unidirectional, refer to Figure 2.1.

In this idealized case, the undeformed top-sheet's velocity would be simply given by

$$\mathbf{v} = v_0 \mathbf{e}_\mathrm{x}, \tag{2.35}$$

where v_0 is the (reference) belt speed, related to the drum's angular velocity. However, when the sheet is deformed, this uniform velocity field no longer applies, and adjustments are necessary to account for the deformed geometry.

A possible way to achieve this is presented in the following. First, the following assumptions are made about the velocity field:

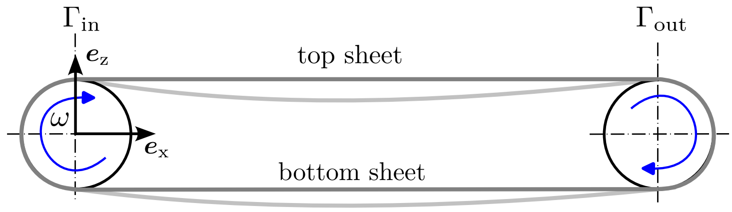

Figure 2.1: Illustration of an idealized belt drive. In practice, the top and bottom sheet may be significantly deformed depending on the specific configuration, the applied external forces and the amount of pre-tension.

1. The incompressibility condition, which was already used for the derivation of the convection-diffusion equation, has to be fulfilled.
2. The velocity field has to be *irrotational*, i.e.,

$$\nabla \times \boldsymbol{v} = 0. \tag{2.36}$$

Using both conditions yields *Laplace's equation*

$$\nabla \cdot \boldsymbol{v} = \nabla \cdot \nabla \Psi = \nabla^2 \Psi = 0, \tag{2.37}$$

where Ψ is the *velocity potential*. In the context of fluid mechanics, this describes a well-studied class of flows, known as *potential flows* [6].

To set the boundary conditions, the additional assumption is made that the velocity is always tangential to the reference plane of the shell, see Figure 2.2.

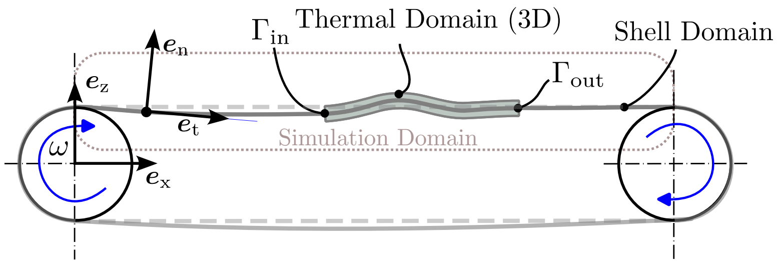

Figure 2.2: Coupling of the mechanical problem (shell domain) and the thermal problem.

Then, the boundary conditions can be set as follows, see Figure 2.3.

- On the inflow boundary Γ_{in} of the sheet it is assumed that $\nabla\Psi \cdot \boldsymbol{n} = -v_0$.
- On the tangential boundaries (top, bottom, left, right) the velocity may be tangential $\nabla\psi \cdot \boldsymbol{n} = 0$, which is the natural BC.
- On the outflow boundary Γ_{out} the potential is fixed (Dirichlet BC).

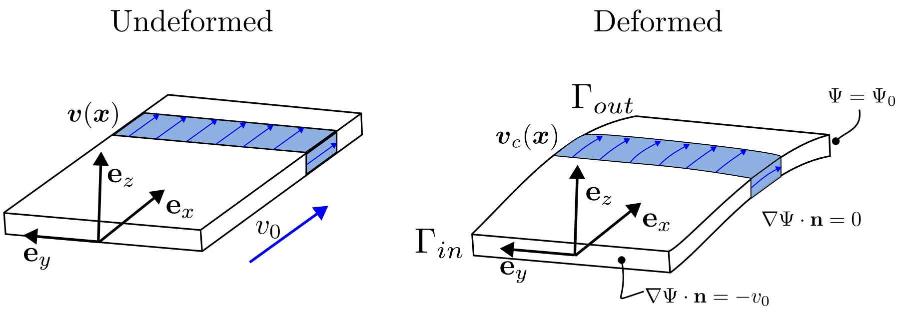

Figure 2.3: Boundary conditions for Laplace's equation

The boundary conditions on Γ_{in} and Γ_{out} can also be swapped. In that case, $\nabla\Psi \cdot \boldsymbol{n} = v_0$ should be set on Γ_{out}.

Similar to the convection-diffusion problem, a weak formulation can be obtained from the strong form. Again, the problem's PDE (2.37) is multiplied with a test function Ψ' and integrated over the whole domain

$$\int_{\Omega} \Psi' \nabla^2 \Psi d\Omega = 0, \tag{2.38}$$

Next, the boundary conditions are incorporated in (2.38), by using Green's first identity[6]

$$\int_{\Omega} \nabla\Psi' \nabla\Psi d\Omega = -\int_{\Gamma_{\text{in}}} \Psi' v_0 d\Gamma. \tag{2.39}$$

From the weak form, again a linear static system can be found using Galerkin's method. As this was already presented in detail for the convection-diffusion equation this will be omitted here.

[6]Refer to the Appendix in [5].

3 Velocity-Related Temperature Error in Deformed Sheets

The goal of this chapter is to compare the temperature field of a deformed sheet under two different velocity assumptions. In the first case, the *uncorrected* scenario, a constant velocity is incorrectly assumed as input for the heat conduction problem. In the second case, the *corrected* scenario, a *conforming* velocity is assumed. This is the case when applying the additional *correction* step, presented in section 2.2.

To understand the effects of different velocity fields on the temperature distribution, a straightforward approach is to compute both cases for a specific simulation problem and then compare the resulting temperature fields. However, to gain a more general understanding of the differences between the two cases, another approach is followed here: both cases are investigated on a relatively general setup using energy balances. Next, this result is simplified for a cross-section in the longitudinal direction. This yields a simple expression that relates the thickness-averaged temperature error with deformation and the difference between the top and bottom surfaces. Then, a scenario is considered where this temperature difference acts only on limited sections of a sheet. Outside these critical sections, the thickness-averaged temperature error remains constant. Using this assumption, a simple expression is derived to relate peak temperature difference and deformation on such sections to the accumulated thickness-averaged temperature error.

3.1 Comparison of Energy-Balances for 3D Problem

To investigate the corrected and uncorrected case for a relatively general thermal belt simulation, the following model is proposed here, refer to Figure 3.1.

The following assumptions are made for both cases:

- The inflow temperatures are equal and fixed to $T_{\mathrm{in}}(y,z)$ (Dirichlet BC).
- A general Neumann BC is applied
$$\int_{\Gamma_{\mathrm{n}}} q_{\mathrm{n}} d\Gamma. \tag{3.1}$$
- A general volumetric power density is applied
$$\int_{\Omega} \dot{q} d\Omega. \tag{3.2}$$
- Heat transfer on top- and bottom surfaces, with heat transfer coefficient α and ambient temperature T_∞; side surfaces are neglected (thin sheet).
- Additionally, it is assumed that the in- and outflow boundaries are parallel to the y-z plane.

Now, the two cases differ as follows:

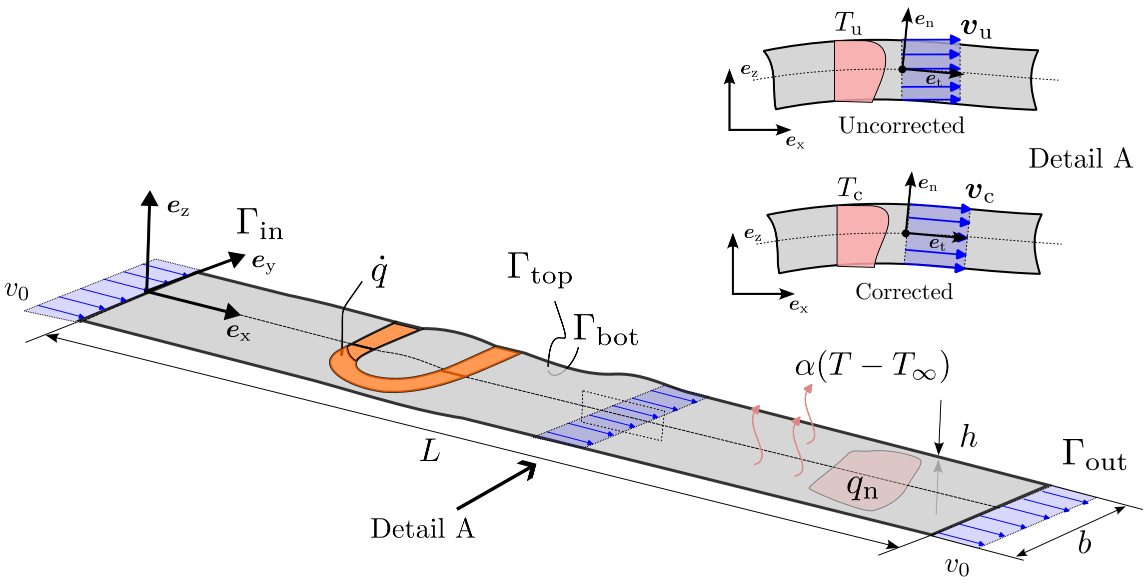

Figure 3.1: Sketch of the thermal setup.

1. The uncorrected velocity field is not adapted to the deformed geometry, and reads,

$$\boldsymbol{v}_\mathrm{u} = v_0 \boldsymbol{e}_\mathrm{x}. \tag{3.3}$$

   The *uncorrected* temperature field is denoted as T_u.

2. The corrected velocity field, which conforms to the deformed geometry, is given by

$$\boldsymbol{v}_\mathrm{c} = v_0 \boldsymbol{e}_\mathrm{t}, \tag{3.4}$$

   where it is assumed the velocity is normal to in- and outflow boundary and tangential on all other boundaries. The *corrected* temperature field is denoted as T_c.

The difference between the resulting temperature fields is denoted as

$$\Delta T := T_\mathrm{u} - T_\mathrm{c}, \tag{3.5}$$

as will be shown, this *temperature error* accumulates along the direction of motion and depends on deformation and belt speed. To arrive at an expression for the average temperature error at the outflow boundary, the energy balances need to be derived for both cases.

First, by applying the energy balance (2.5), to the corrected case, the following can be found

$$\rho c_\mathrm{p} \int_{\partial\Omega} T_\mathrm{c} (\boldsymbol{v}_\mathrm{c} \cdot \boldsymbol{n}) d\Gamma = \int_\Omega \dot{q} d\Omega + \int_{\Gamma_\mathrm{n}} q_\mathrm{n} d\Gamma - \int_{\Gamma_\mathrm{top} \cup \Gamma_\mathrm{bot}} \alpha (T_\mathrm{c} - T_\infty) d\Gamma. \tag{3.6}$$

Analogously, the energy balance for the *uncorrected* case leads to

$$\rho c_\mathrm{p} \int_{\partial\Omega} T_\mathrm{u} (\boldsymbol{v}_\mathrm{u} \cdot \boldsymbol{n}) d\Gamma = \int_\Omega \dot{q} d\Omega + \int_{\Gamma_\mathrm{n}} q_\mathrm{n} d\Gamma - \int_{\Gamma_\mathrm{top} \cup \Gamma_\mathrm{bot}} \alpha (T_\mathrm{u} - T_\infty) d\Gamma. \tag{3.7}$$

Next, the convective term in (3.6), is simplified to

$$\int_{\partial\Omega} T_\mathrm{c} (\boldsymbol{v}_\mathrm{c} \cdot \boldsymbol{n}) d\Gamma = v_0 b h (\bar{T}_\mathrm{c,out} - \bar{T}_\mathrm{in}), \tag{3.8}$$

where $\bar{T}_{\mathrm{c,out}}$ and $\bar{T}_{\mathrm{in}}$ are averaged temperatures over the out- and inflow boundary, respectively.

Again, this step is repeated for the uncorrected convective term in (3.7), leading to

$$\int_{\partial\Omega} T_{\mathrm{u}}(\boldsymbol{v}_{\mathrm{u}} \cdot \boldsymbol{n}) d\Gamma = v_0 bh(\bar{T}_{\mathrm{u,out}} - \bar{T}_{\mathrm{in}}) + v_0 \int_{\Gamma_{\mathrm{top}} \cup \Gamma_{\mathrm{bot}}} T_{\mathrm{u}} \underbrace{(\boldsymbol{e}_{\mathrm{x}} \cdot \boldsymbol{n})}_{:=n_{\mathrm{x}}} d\Gamma \tag{3.9}$$

where now erroneous terms, for the top- and bottom surfaces, occur.

Using (3.9), the energy balance for the uncorrected case reads

$$\begin{aligned} v_0 \rho c_{\mathrm{p}} bh(\bar{T}_{\mathrm{u,out}} - \bar{T}_{\mathrm{in}}) + v_0 \rho c_{\mathrm{p}} \int_{\Gamma_{\mathrm{top}} \cup \Gamma_{\mathrm{bot}}} T_{\mathrm{u}} n_{\mathrm{x}} &= \int_{\Omega} \dot{q} d\Omega + \int_{\Gamma_{\mathrm{n}}} q_{\mathrm{n}} d\Gamma \\ &- \int_{\Gamma_{\mathrm{top}} \cup \Gamma_{\mathrm{bot}}} \alpha(T_{\mathrm{u}} - T_{\infty}) d\Gamma, \end{aligned} \tag{3.10}$$

and for the corrected case

$$v_0 \rho c_{\mathrm{p}} bh(\bar{T}_{\mathrm{c,out}} - \bar{T}_{\mathrm{in}}) = \int_{\Omega} \dot{q} d\Omega + \int_{\Gamma_{\mathrm{n}}} q_{\mathrm{n}} d\Gamma - \int_{\Gamma_{\mathrm{top}} \cup \Gamma_{\mathrm{bot}}} \alpha(T_{\mathrm{c}} - T_{\infty}) d\Gamma. \tag{3.11}$$

Now, by subtracting the energy balances (3.10) from (3.11), the following expression can be found

$$\bar{T}_{\mathrm{u,out}} - \bar{T}_{\mathrm{c,out}} = -\frac{1}{bh\rho c_{\mathrm{p}} v_0} \int_{\Gamma_{\mathrm{top}} \cup \Gamma_{\mathrm{bot}}} \alpha(T_{\mathrm{u}} - T_{\mathrm{c}}) d\Gamma - \frac{1}{bh} \int_{\Gamma_{\mathrm{top}} \cup \Gamma_{\mathrm{bot}}} T_{\mathrm{u}} n_{\mathrm{x}} d\Gamma, \tag{3.12}$$

which leads to the definition of the averaged temperature error at the outflow boundary

$$\Delta \bar{T}_{\mathrm{out}} = \bar{T}_{\mathrm{u,out}} - \bar{T}_{\mathrm{c,out}}. \tag{3.13}$$

In the following section the result (3.12) is further simplified by investigating the problem only on cross-sections parallel to the x-z plane. Hereafter, such a cross-section is called a *slice*, see Figure 3.3.

3.2 A Simplified One-Dimensional Model

Let,

$$C_{\mathrm{tb}} = C(\Gamma_{\mathrm{top}} \cup \Gamma_{\mathrm{bot}}), \tag{3.14}$$

denote the top and bottom boundary curve of a slice. Then, the surface integrals in (3.12) reduce to line integrals. Moreover, it is assumed that the difference between deformed and undeformed curve length L is small, such that a line integral can be approximated with an integral over axial coordinate x and that the heat transfer coefficient is constant and equal on both sides. By using these assumptions, the heat transfer term in (3.12), can be simplified to

$$\int_{C_{\mathrm{tb}}} \alpha(T_{\mathrm{u}} - T_{\mathrm{c}}) ds \approx \alpha \int_0^L \left(\Delta T_{\mathrm{top}}(x) + \Delta T_{\mathrm{bot}}(x)\right) dx, \tag{3.15}$$

where ΔT_{top} and ΔT_{bot} are the temperature errors evaluated on the top and bottom respectively.

The error source term in (3.12) yields

$$\int_{C_{\mathrm{tb}}} T_{\mathrm{u}} n_{\mathrm{x}} ds \approx \int_0^L T_{\mathrm{u,top}} n_{\mathrm{x,top}} dx + \int_0^L T_{\mathrm{u,bot}} n_{\mathrm{x,bot}} x dx. \tag{3.16}$$

Next, it is assumed that the deformation in z-direction, on the mid-surface plane, is given by

$$w(x), \tag{3.17}$$

and that the typical assumptions of geometrically linearized mechanics apply.

Moreover, the deformation is such that, the top and bottom normal vectors are equal and opposite

$$\boldsymbol{n}_{\text{top}} = -\boldsymbol{n}_{\text{bot}}. \tag{3.18}$$

Then, the x-component of the normal vectors can be found to be

$$n_{\text{x,top}} = -n_{\text{x,top}} = -w'(x), \tag{3.19}$$

which finally yields,

$$\int_0^L T_{\text{u,top}} n_{\text{x,top}} dx + \int_0^L T_{\text{u,bot}} n_{\text{x,bot}} dx = -\int_0^L \Delta T_{\text{u,tb}} w' dx, \tag{3.20}$$

where the difference between top and bottom temperature for the uncorrected case, was now defined as

$$\Delta T_{\text{u,tb}} := T_{\text{u,top}} - T_{\text{u,bot}}. \tag{3.21}$$

Collecting the now simplified terms, in (3.15) and (3.20), results in

$$\Delta \bar{T}(x = L, y = y_{\text{s}}) = \frac{1}{h} \int_0^L \Delta T_{\text{u,tb}} w' dx - \frac{\alpha}{h \rho c_{\text{p}} v_0} \int_0^L (\Delta T_{\text{top}} + \Delta T_{\text{bot}}) dx, \tag{3.22}$$

which is the curve[1] averaged error over the outflow contour, for a slice at position y_{s}.

In the second term, the Stanton number[2] can be identified as

$$\text{St} := \frac{\alpha}{\rho c_{\text{p}} v_0}, \tag{3.23}$$

leading to

$$\Delta \bar{T}(x = L, y = y_{\text{s}}) = \frac{1}{h} \int_0^L \underbrace{\Delta T_{\text{u,tb}} w'}_{:= f_{\text{u}}} dx - \frac{\text{St}}{h} \int_0^L (\Delta T_{\text{top}} + \Delta T_{\text{bot}}) dx. \tag{3.24}$$

Before proceeding further, two observations can be made about (3.24):

1. The integral containing $f_{\text{u}} = \Delta T_{\text{u,tb}} w'$ can be considered the error *forcing* term. Only sections where significant deformation *and* temperature gradients in the thickness direction occur, are contributing to the downstream thickness-averaged temperature error $\Delta \bar{T}$.
2. The heat transfer related term, which contains the temperature error at the top ΔT_{top} and bottom interface ΔT_{bot}, may lead to a reduction of a given error. However, this term is scaled by the Stanton number, which in the considered applications is relatively small, see Figure 3.2. This term will be neglected for the subsequent derivations.

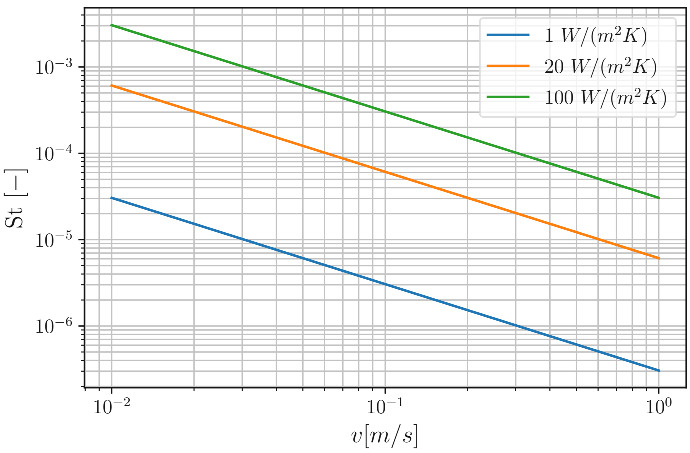

Figure 3.2: Heat transfer and speed dependence of the Stanton number for a typical steel belt application. Material values are given in Table 4.2.

To arrive at an expression for the thickness-averaged error at an arbitrary position x, it is assumed that the outflow boundary is variable, and that heat transfer is negligible. Similar to Equation 3.24, this leads to

$$\Delta\bar{T}(x) = \frac{1}{h}\int_0^x \Delta T_{\mathrm{u,tb}} w' d\xi, \tag{3.25}$$

now at position x. Furthermore, the derivative of (3.25) yields a local error rate

$$\frac{d\Delta\bar{T}}{dx} = \frac{\Delta T_{\mathrm{u,tb}} w'}{h} = \frac{f_{\mathrm{u}}}{h}. \tag{3.26}$$

3.3 Error Section Model

To find the thickness-averaged temperature error, the expression (3.25) has to be evaluated. Without solving the heat equation for the uncorrected problem, the term $\Delta T_{\mathrm{u,tb}}$ is still unknown.

However, because the sheet is very thin, the temperature difference $\Delta T_{\mathrm{u,tb}}$ may be limited to sections of a sheet where, for example, significant Joule losses occur. Outside, of these sections, the difference may quickly average out due to diffusion in thickness direction. This observation motivates the introduction of the *error section model*, see Figure 3.3. Additional to the assumptions of the last section, the assumption is made that, $\Delta T_{\mathrm{u,tb}} = 0$ outside such *error* sections. This leads to the following equation

$$\Delta\bar{T}(L) = \frac{1}{h}\sum_{m=1}^{M}\int_{\Delta x_m} f_{\mathrm{u},m} dx = \sum_{m=1}^{M} F_{\mathrm{u},m}, \tag{3.27}$$

were the problem is now reduced to finding relations for the error contributions $F_{\mathrm{u},m}$ of each section, i.e., evaluating

[1]For simplicity, $\Delta\bar{T}$ will represent either the surface or curve average, with the meaning typically clear from the context.

[2]The Stanton number represents the ratio of heat transferred into a body to the thermal capacity of the body [10].

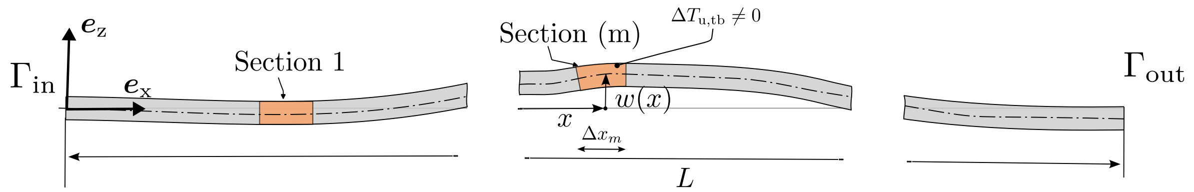

Figure 3.3: A 2D slice of the 3D sheet: *sections* are intervals where temperature differences between top and bottom are significant, outside these sections they are assumed to be negligible.

$$F_{u,m} = \int_{\Delta x_m} T_{u,tb} w' dx, \tag{3.28}$$

with section length $\Delta x_m := x_m - x_{m-1}$.

Analagously, the accumulated error at x can be given as a piecewise-constant function. This is done by assigning the accumulated error of each section to the section center[3]. Using the Heaviside function $\Theta(x)$, this reads

$$\Delta\bar{T}(x) = \frac{1}{h} \sum_{m=1}^{M} F_{u,m} \Theta_m. \tag{3.29}$$

where $\Theta_m := \Theta(x - x_{m/2})$ is defined as a step function at the center $x_{m/2}$ of the error-section.

The shape of $f_{u,m}$, is typically also unknown. However, by approximating the integral as

$$\int_{\Delta x_m} f_{u,m} dx \approx \pm C_m \Delta x_m \hat{T}_{u,tb(m)} \hat{w'}_{(m)},, \tag{3.30}$$

a relation to the (possibly estimated) peak values of $\hat{T}_{tb(m)}$ and $\hat{w'}_{(m)}$ can be given. The additional weighting parameter $C_m \in [0, 1]$, depends on the shape of $f_{u,m}$. For a cosine-like shape $C \approx 0.5$, and if constant values are assumed $C = 1$.

[3]The error of a section could also be assigned to the beginning or end of the section.

4 Parameter Study in 2D Model

As demonstrated in the previous chapter, an unadapted velocity field for a deformed sheet can lead to erroneous energy influx due to temperature gradients in the thickness direction. These temperature gradients typically arise from uneven heating, such as Joule losses concentrated near the top surface. Outside these critical sections, gradients dissipate due to diffusion, and the thickness-averaged temperature error may not increase significantly.

The goal of this chapter is to investigate the error behavior and gradient dissipation after a critical section, such as an inductor zone.

By setting a known temperature gradient at the inflow boundary and controlling the deformation of a short section, the development of the gradient along the direction of motion and its influence on the thickness-averaged error can be analyzed in a numerical experiment. Because these effects depend on deflection, speed, and heat transfer, this is investigated in a parameter study.

Additionally, a simple parametric model is introduced that may be used to describe the decay of the temperature difference in thickness-direction. This leads to a simple expression as a function the belt's speed and the diffusion coefficient of the material. Assuming the validity of this model, an analytical expression for the thickness-averaged temperature error was found and is also compared with the numerical results.

4.1 Description

The simulation domain is a rectangular shape with length L and height h. This represents a slice of a sheet. The mesh is continuously deformed, by applying a known displacement on the center line, see Figure 4.1.

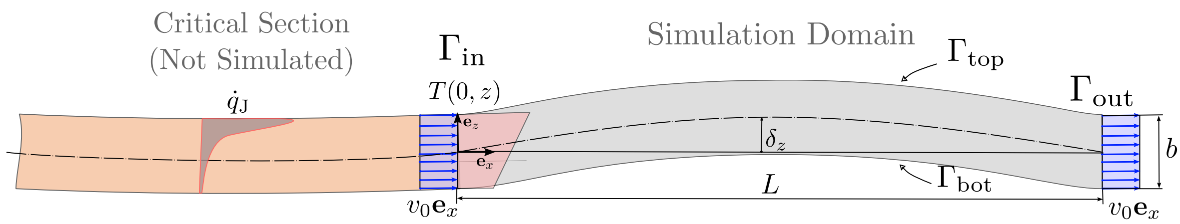

Figure 4.1: Sketch of the simulation model (not to scale). A critical section introduces uneven heating and leads to a temperature gradient. This gradient, which is assumed to be linear here, is the inflow BC of the simulation model.

For the displacement the following expression was chosen

$$w(x, z = 0) = \delta_z \sin^2 \frac{x\pi}{L}, \tag{4.1}$$

where δ_z is the maximum deflection.

The deformation of the mesh is achieved by solving a grid smoothing problem with $w(x, z = 0)$ applied as BC on the center line and fixing the nodes on Γ_{in} and Γ_{out}.

For the corrected velocity field, the Laplace equation for the velocity potential is solved on the deformed geometry using the following boundary conditions:

- On the outlet boundary (Γ_{out}):
$$\nabla\psi \cdot \mathbf{n} = v_0. \tag{4.2}$$
- The inlet boundary (Γ_{in}) is set to a Dirichlet BC with
$$\psi = 0. \tag{4.3}$$

The thermal boundary conditions are set as follows:

- The inlet boundary (Γ_{in}) has the prescribed linear temperature profile
$$T(x = 0, z) = \bar{T}_{\text{in}} + \Delta T_{\text{tb,in}} \frac{z}{h}. \tag{4.4}$$
- The outlet boundary (Γ_{out}) is set to a Neumann BC with $q_{\text{n}} = 100\,\text{W}\,\text{m}^{-2}$.
- The top and bottom boundaries (Γ_{top} and Γ_{bot}) may be subject to heat transfer with the ambient environment, or are thermally insulated if $\alpha = 0$.

All three sub-problems (deformation, velocity correction, heat conduction) are solved using FEM schemes implemented in openCFS [11].

4.2 A Parametric Model for the Thickness-Averaged Temperature Error

To determine the thickness-averaged temperature error, it was shown in section 3.3 that the following integral needs to be evaluated:

$$\Delta\bar{T}(x) = \frac{1}{h}\int_0^x T_{\text{u,tb}} w' \, d\xi. \tag{4.5}$$

Given that the deformation is already expressed analytically, the remaining task is to find an expression for the temperature difference $T_{\text{u,tb}}(x)$. For the given problem, $T_{\text{u,tb}}(x)$ is not constant but varies along x. The question arises whether a simple parametric model for $\Delta\bar{T}(x)$ can be found. For this, it is assumed that the temperature difference can be modelled in the following form:

$$\Delta\tilde{T}_{\text{u,tb}}(x) = f(x, h, v_0, \kappa)\Delta T_{\text{tb,in}}, \tag{4.6}$$

where $\Delta\tilde{T}_{\text{u,tb}}$ denotes the approximation of ΔT_{tb}. Furthermore, heat transfer is not considered in this model.

Using dimensional analysis (refer to [9] for background), the number of arguments in f can be reduced by introducing a dimensionless coordinate:

$$\tilde{x} = \frac{x}{h}, \tag{4.7}$$

and the Peclet number:

$$\text{Pe} = \frac{v_0 h}{\kappa}, \tag{4.8}$$

resulting in:

$$f(x, h, v_0, \kappa) = \tilde{f}(\tilde{x}, \mathrm{Pe}). \tag{4.9}$$

To satisfy the inflow boundary condition, the following should be fulfilled

$$\tilde{f}(0, \mathrm{Pe}) = 1. \tag{4.10}$$

Additionally, for increasing Peclet numbers (e.g., due to higher velocities), it is assumed that the temperature difference is transported farther into the domain. This assumption can be captured by:

$$\mathrm{Pe}_A > \mathrm{Pe}_B \implies \tilde{f}(\tilde{x}, \mathrm{Pe}_A) > \tilde{f}(\tilde{x}, \mathrm{Pe}_B). \tag{4.11}$$

These conditions are satisfied by the function:

$$\tilde{f} = \exp\left(-C\mathrm{Pe}^{-1}\tilde{x}\right), \tag{4.12}$$

with a yet-to-be-determined factor C. Using this function, the approximation for the temperature difference between the top and bottom surfaces is:

$$\Delta\tilde{T}_{\mathrm{u,tb}}(x) = \Delta T_{\mathrm{tb,in}} \exp\left(-C\mathrm{Pe}^{-1}\tilde{x}\right) = \Delta T_{\mathrm{tb,in}} \exp\left(-Cx/L_{\mathrm{D}}\right), \tag{4.13}$$

where the characteristic diffusion length is:

$$L_{\mathrm{D}} = \frac{vh^2}{\kappa}. \tag{4.14}$$

Finally, with expressions for both ΔT_{tb} and w available, (4.5) can be evaluated, resulting in:

$$\Delta\bar{T}(x) = \frac{\Delta T_{\mathrm{tb,in}}\delta_z}{h} \frac{2\pi^2}{(Lc)^2 + (2\pi)^2} \left[1 - e^{-cx}\left(\cos\frac{2\pi x}{L} + \frac{Lc}{2\pi}\sin\frac{2\pi x}{L}\right)\right], \tag{4.15}$$

with:

$$c = C\frac{\kappa}{vh^2}. \tag{4.16}$$

If (4.15) is evaluated at the outflow, the formula simplifies to:

$$\Delta\bar{T}(L) = \frac{\Delta T_{\mathrm{tb,in}}\delta_z}{h} \frac{2\pi^2}{(Lc)^2 + (2\pi)^2} \left(1 - e^{-cL}\right). \tag{4.17}$$

For the range of parameters investigated, the tuning parameter C was found to be in the range of 10-20, with 14 chosen as a compromise.

4.3 Experiment Methodology

The methodology for the parameter study involves setting up a series of simulations with varying parameters, see Figure 4.2.

The steps involved are as follows:

1. Define the geometry and material properties of the 2D model.
2. Vary the parameters systematically to cover the range of interest.
3. Run the simulations and collect the data.

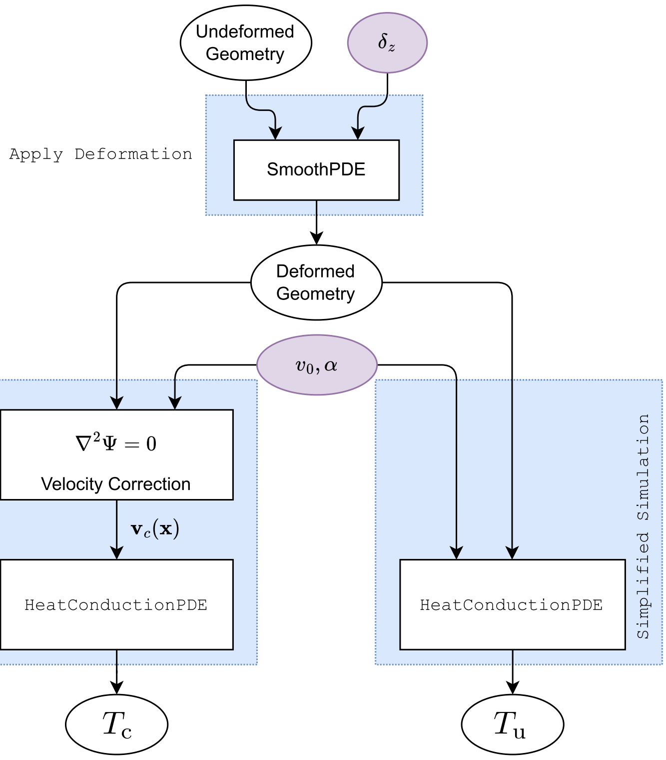

Figure 4.2: Overview of experiment procedure

Table 4.1: Parameters for 2D experiment

	Symbol	Value	Unit
Length	L	300	mm
Thickness	h	1	mm
Max. Deflection	δ_z	1-10	mm
Speed	v_0	0.1-1	$\mathrm{m\,s^{-1}}$
Heat Transfer Coefficient	α	$\{0, 20\}$	$\mathrm{W\,m^{-2}\,K^{-1}}$
Ambient Temp.	T_∞	20	°C
Inflow Temp. Avg.	$\bar{T}_{\mathrm{in}}$	55	°C
Inflow Temp. Difference	$\Delta T_{\mathrm{tb,in}}$	10	K

4. Analyze the results to determine the influence of each parameter on the velocity-related temperature error.

The parameters include the length of the model, the thickness, the maximum deflection, the speed, and the heat transfer coefficient and are shown in Table 4.1.

The material data was taken from the specifications of a steel used in an industrial steel belt, see Table 4.2.

Table 4.2: Material data for 2D experiment

	Symbol	**Value**	**Unit**
Density	ρ	7800	$\mathrm{kg\,m^{-3}}$
Young's Modulus	E	210	GPa
Poisson's Ratio	ν	0.3	-
Heat Capacity	c_p	510	$\mathrm{J\,m^{-3}\,K^{-1}}$
Heat Conductivity	k	15	$\mathrm{W\,m^{-1}\,K^{-1}}$

4.4 Results

In the following section, the results of the parameter study are presented. First, to illustrate the parameter dependence of the "true" outflow error $\Delta T(L)$, the results from the FEM simulations are presented. Next, for a subset of the parameter combinations, true and estimated errors are compared. Finally, to show how the involved quantities develop along x, detailed results are compared for two selected sets of parameters.

The nomenclature is defined as follows:

- *FEM*: Refers to the results from the FE simulation.
- *1D-M($\Delta T_{u,tb}$)*: Refers to (3.25), with $\Delta T_{\mathrm{u,tb}}$ taken from the uncorrected FE simulation and w' computed from (4.1). The integral in (3.25) was evaluated numerically using a midpoint scheme.
- *Analytic*: Refers to the analytical error approximation (4.15).

Parameter-Dependence of FEM Outflow Error

The parameter dependence of the outflow error $\Delta\bar{T}(L)$ was computed using the presented methodology. The results are shown in Figure 4.3.

It can be observed that the error increases with increasing speed and deflection. The errors are generally higher when heat transfer is not acting on the top and bottom. Moreover, with rising parameters (v_0, δ_z) the error increase is more pronounced in the case without heat transfer.

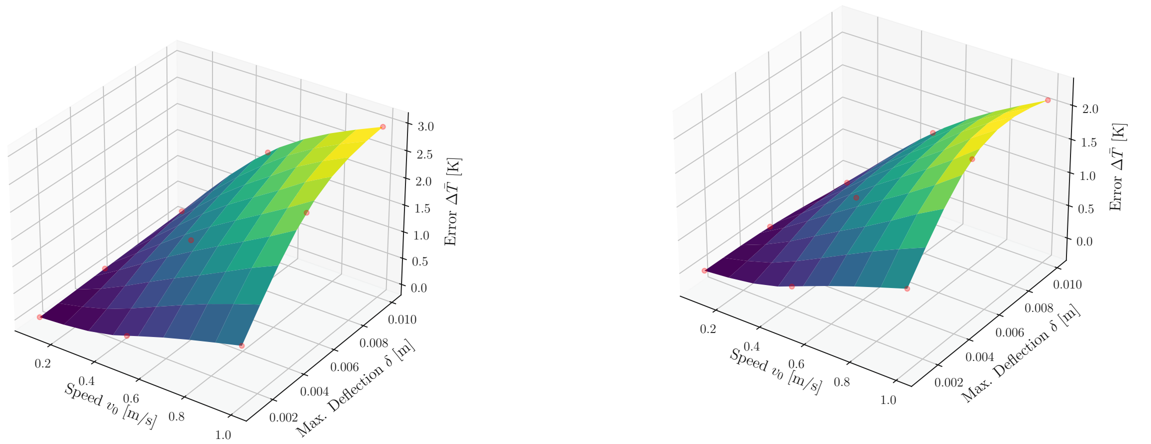

(a) Without heat transfer

(b) Including heat transfer with $\alpha = 20\,\mathrm{W/(m^2K)}$

Figure 4.3: Comparison of the outflow error $\Delta\bar{T}(L)$ computed from FEM results.

Comparison of Analytical Error Estimate

A subset of parameter combinations was investigated further, by only considering a deflection δ_z of 10 mm, which corresponds to 9 samples. For these, the outflow $\Delta\bar{T}(L)$ and maximum error

$$\max_x \Delta\bar{T}(x), \tag{4.18}$$

was compared with the analytical approximation. The results are depicted in Figure 4.4. As

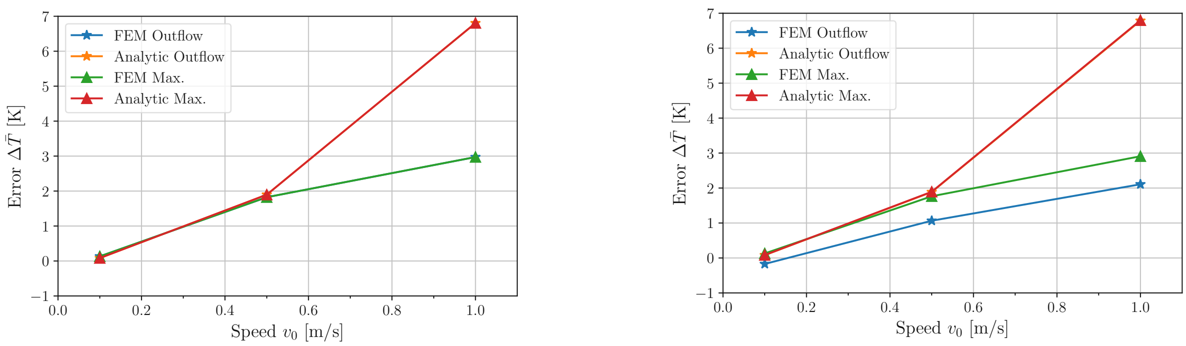

(a) Without heat transfer

(b) Including heat transfer with $20\,\mathrm{W/(m^2K)}$

Figure 4.4: Comparison of the outflow error $\Delta\bar{T}(L)$ and maximum error of $\Delta\bar{T}(x)$ at a deflection of $\delta_z = 10\,\mathrm{mm}$.

can be observed in Figure 4.4a, if no heat transfer is involved, the maxima and outflow errors are identical. The analytical error approximation (4.15) is in good agreement with the FEM error up to 0.5 m/s, but is deviating above. By increasing the tuning parameter C, which was set to 14 here, this can be improved, with the sacrifice of worse performance for lower speeds.

Now, it is notable that, if heat transfer is included, see Figure 4.4b, the error maxima are unchanged, only the outflow errors are reduced (and even become slightly negative for the lowest error case).

Detailed Results along Axial Coordinate

To investigate how the errors and involved quantities develop along the axial coordinate, detailed results for a parameter set without heat transfer are shown in Figure 4.5. For the uncorrected

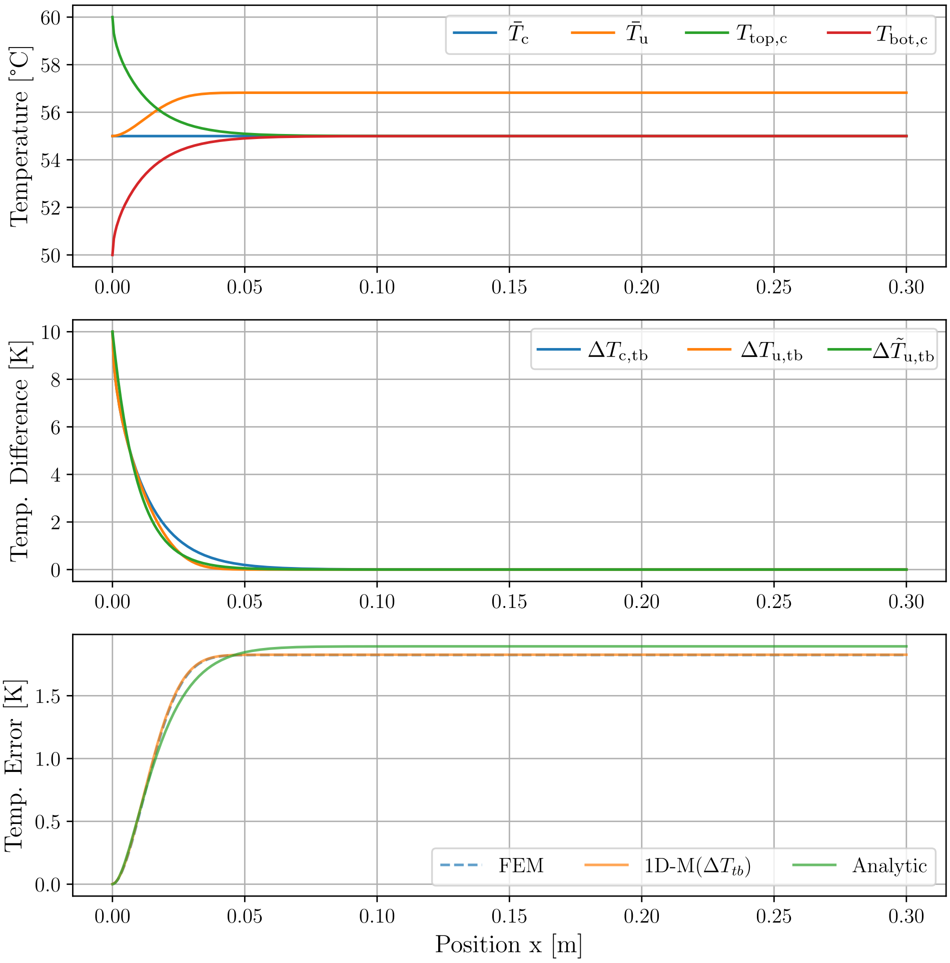

Figure 4.5: Detailed results for $\alpha = 0\,\mathrm{W/(m^2K)}$, $\delta_z = 10\,\mathrm{mm}$ and $v_0 = 0.5\,\mathrm{m/s}$.

case, the temperature $\bar{T}_\mathrm{u}$ rises, because w' is positive, and the top temperature is higher than the bottom temperature: $\Delta T_\mathrm{u,tb} > 0$. For the corrected case, the thickness-averaged temperature stays constant, as no energy is added to the system.

A key finding is that, the resulting temperature error only increases until ca. 3 cm, after which it stays constant. This effect was already observed in Figure 4.4a. This can be explained by the diffusion in thickness direction. The prescribed temperature difference at the inflow boundary, vanishes along x: even tough a deformation is present, no additional error in average temperature is made.

Moreover, it can be observed that the parametric model for $\Delta\tilde{T}_\mathrm{tb}(x)$ is in acceptable agreement. Lastly, it can be pointed out that, by knowing the forcing term precisely, *1D-M(ΔT_{tb})* yields the same results as the error directly computed from the FEM simulation.

In comparison with Figure 4.5, the heat transfer case in Figure 4.6, shows a falling error after the maximum at ca. 3 cm.

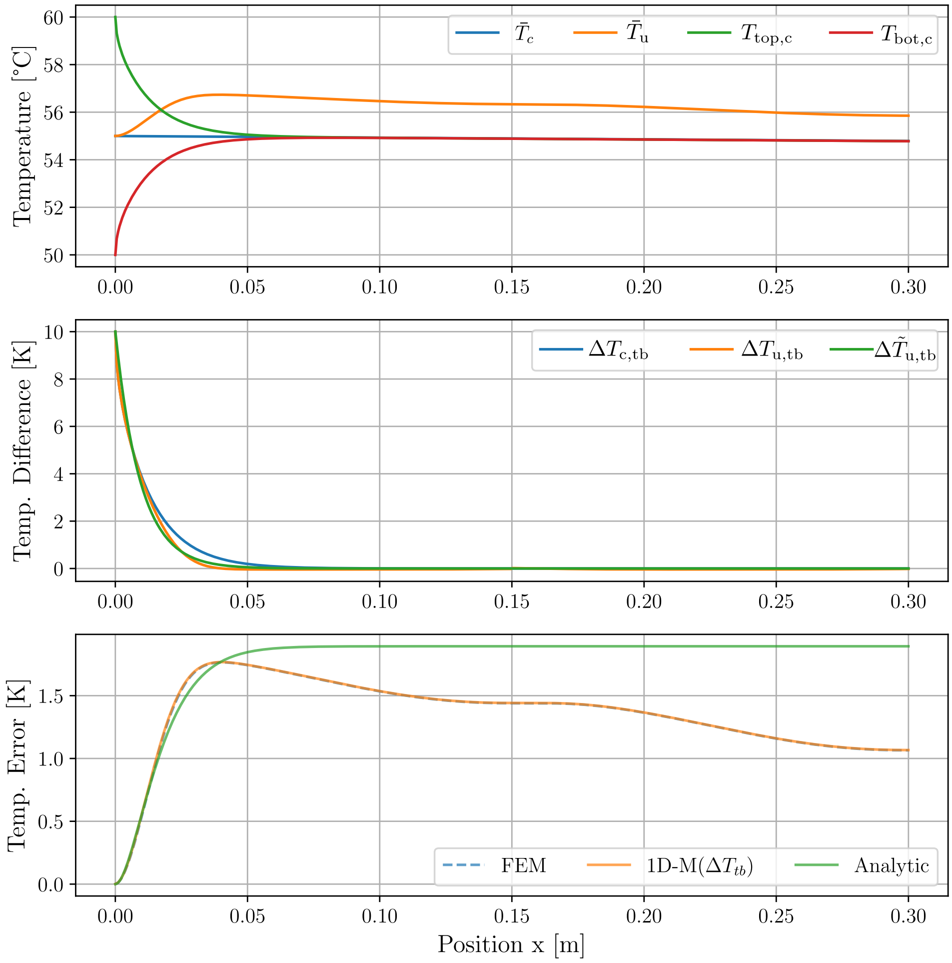

Figure 4.6: Detailed results for $\alpha = 20\,\mathrm{W/(m^2K)}$, $\delta_z = 10\,\mathrm{mm}$ and $v_0 = 0.5\,\mathrm{m/s}$.

5 Validation in Coupled 3D Model

In the last chapter it was shown how the thickness-averaged temperature error behaves in a simple 2D model. This chapter deals with the question, how the errors behave in a more practical setting and how they compare with the error estimated with the error section method.

For this experiment, a model of a steel belt with induction heating was investigated, see Figure 5.1. A similar model was used in [3], where the post-buckling behavior was modelled. Before presenting the results of the FEM simulation and the comparison of errors for a cross-section, it is shown how the error section method can be applied to this setup.

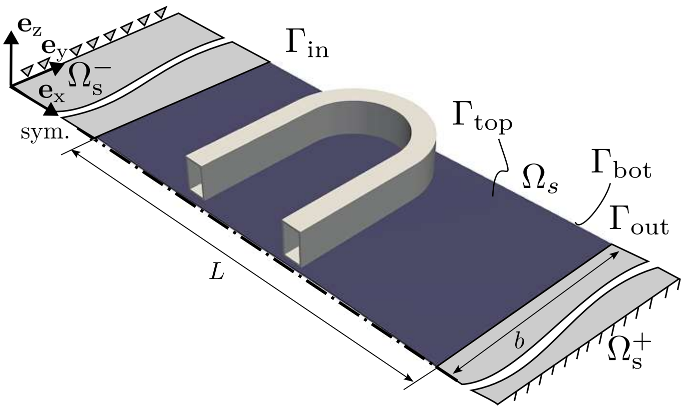

Figure 5.1: Overview of simulation domain and geometry. Inductor and sheet are connected via an air domain (not shown).

5.1 Application of Error Section Method

In the following, it is shown how the error section method, presented in section 3.3, can be applied to the induction heating setup.

First, the problem is reduced to a cross-section slice, see Figure 5.2. For this, the middle x-z plane with $y_s = 0.15\,\mathrm{m}$ was chosen.

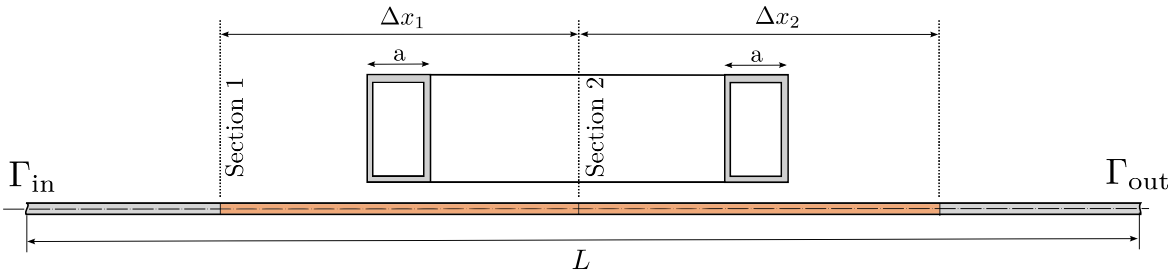

Figure 5.2: Sketch of sheet slice with error sections

Because the Joule losses are concentrated at the top surface, the section under each arm of the inductor can be identified as potential error sections. The Joule losses lead to temperature difference in thickness direction, which makes the zones with significant Joule losses sensitive to errors. It was assumed that the length of significant Joule losses are equal for both sections $m = \{1, 2\}$

$$\Delta x_1 = \Delta x_2 = \Delta x, \tag{5.1}$$

and that they are related to the inductor coil width a via

$$\Delta x = C_\mathrm{J} a, \tag{5.2}$$

where the factor C_J determines the width of the Joule loss zone. In the present experiment it was set to 5.67, which coincidentally leads to overlapping section boundaries.

Moreover, the weighting parameters in (3.30) are assumed to be equal for both sections,

$$C_1 = C_2 = C, \tag{5.3}$$

were a value of 0.4 was chosen and the section error contributions (3.30) take the form

$$F_{\mathrm{u},m} = C \Delta x \hat{T}_{tb(m)} \hat{w'}_{(m)}, \tag{5.4}$$

where $\hat{T}_{tb(m)}$ and $\hat{w'}_{(m)}$ are the maxima in each section. To finalize, the error section approximation for this setup is now given by

$$\Delta \bar{T}(x) = \frac{C \Delta x}{h} \left(\hat{T}_{tb(1)} \hat{w'}_{(1)} \Theta_1 + \hat{T}_{tb(2)} \hat{w'}_{(2)} \Theta_2 \right), \tag{5.5}$$

where Θ_1 and Θ_2 are step functions assigned to the section center, i.e. the center of each inductor arm.

5.2 Experiment Description

The full simulation, consists of the following steps (refer to Figure 5.3):

1. **Deformation** (see Figure 5.3a) This step was based on the method presented in [3].
   a) Compute the electromagnetic (EM) field, by solving the eddy-current problem in the frequency domain. For details on the computation of the eddy-current problem, refer to [3]. The system is excited by prescribing a total current of $I = 6.5\,\mathrm{kA}$ at $f = 5\,\mathrm{kHz}$ through the inductor coil. The induced eddy-currents lead to Joule losses. By averaging the Joule losses over a single oscillation period, the volumetric power density $\dot{q}_\mathrm{J}$ for the belt sheet domain Ω_s can be found.
   b) Calculate the temperature field by computing the convection-diffusion equation for given speed v_0 and $\dot{q}_\mathrm{J}$. Here the velocity field was not additionally corrected.
   c) Solve the thermo-mechanical problem, for the given temperature distribution, with a shell FEM. An extended sheet domain $\Omega_\mathrm{B} = \Omega_\mathrm{s}^- \cup \Omega_\mathrm{s} \cup \Omega_\mathrm{s}^+$, with a total length of $2\,\mathrm{m}$, was used. The ends were fixed on one side and vertically clamped on the other.
   d) Apply the shell displacement to the 3D continuum in Ω_s by solving a grid smoothing problem. The resulting deformed geometry can be reused as input for the EM step. Two iteration steps where done here, before proceeding to the *post-deformation* step.
2. **Post-Deformation** (see Figure 5.3b)

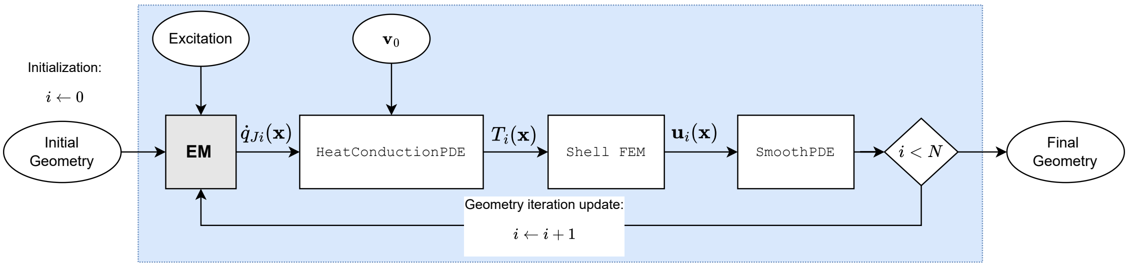

(a) Deformation step, in the experiment N was set to 2.

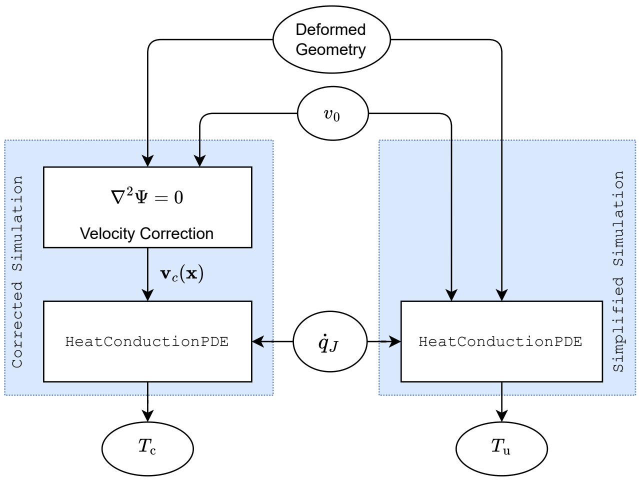

(b) Post-deformation step

Figure 5.3: Overview of the experiment steps.

a) Compute the corrected velocity field on the deformed geometry.

b) Use the Joule losses from the pre-deformation step to compute the corrected and uncorrected temperature field.

The material data is summarized in Table 5.1.

Table 5.1: Material data for 3D simulation

Material Parameter	**Sheet** *Steel*	**Inductor** *Copper*	**Air** -
Magnetic Permeability μ in $\mathrm{H\,m^{-1}}$	1.26×10^{-5}	1.26×10^{-6}	1.26×10^{-6}
Electric Conductivity in $\mathrm{S\,m^{-1}}$	5.96×10^{7}	5.96×10^{7}	
Young's Modulus E in GPa	210		
Poisson's Ratio ν	0.3		
Thermal Expansion Coefficient α_T in $\mathrm{K^{-1}}$	12×10^{-6}		
Density ρ in $\mathrm{kg/m^3}$	7800		
Heat Capacity c_p in $\mathrm{J\,m^{-3}\,K^{-1}}$	510		
Heat Conductivity k in $\mathrm{W\,m^{-1}\,K^{-1}}$	15		

The experiment parameters for the post deformation step can be found in Table 5.2.

Table 5.2: Experiment parameters for post deformation step

Experiment Parameter	**Symbol**	**Value**	**Unit**
Length of Ω_s	L	300	mm
Inductor Coil Width	a	15	mm
Thickness	h	1	mm
Width	b	150	mm
Speed	v_0	0.1	m/s
Heat Transfer Coefficient	α	20	$\mathrm{W/(m^2K)}$
Ambient Temp.	T_∞	20	°C
Inflow Temp. at Γ_in	T_in	60	°C

5.3 FE Simulation Results

In this section, selected results from the FE simulation are presented. The temperature distribution and temperature difference between the top and bottom surfaces are shown in Figure 5.4a and Figure 5.4b, respectively. The thickness-averaged temperature error and vertical displacement are depicted in Figure 5.4c and Figure 5.4d.

Additionally, the error source terms along a slice are illustrated in Figure 5.6, and a comparison of the mean temperature along the slice is provided in Figure 5.5.

Discussion

As can be seen in Figure 5.4a, the temperature increases from the constant inflow temperature by ca. 200 °C to 250 °C. Near the coil turn, the energy density decreases rapidly in y-direction,

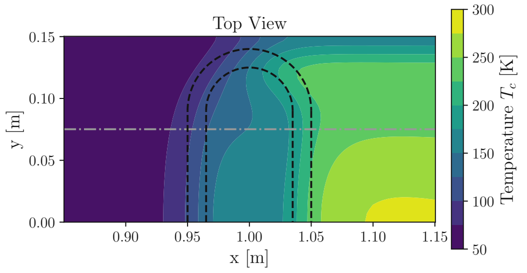

(a) Temperature distribution (corrected)

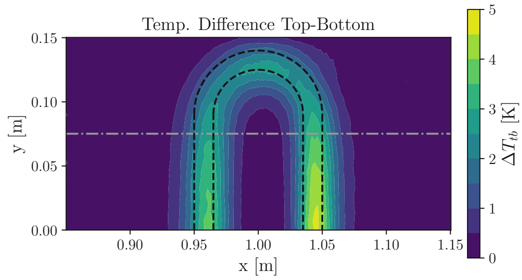

(b) Temp. difference top-bottom (corrected)

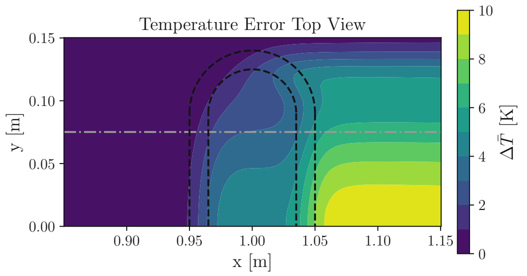

(c) Thickness averaged temperature error

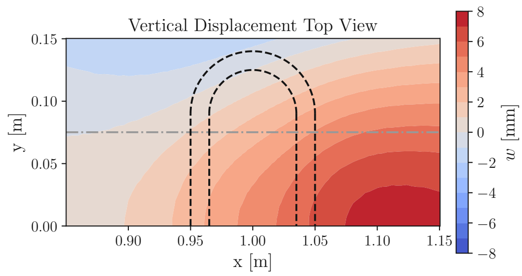

(d) Vertical displacement

Figure 5.4: Selected results from FEM simulation. Dash-dotted line represents position of the slice. Dashed line shows the inductor coil's outline.

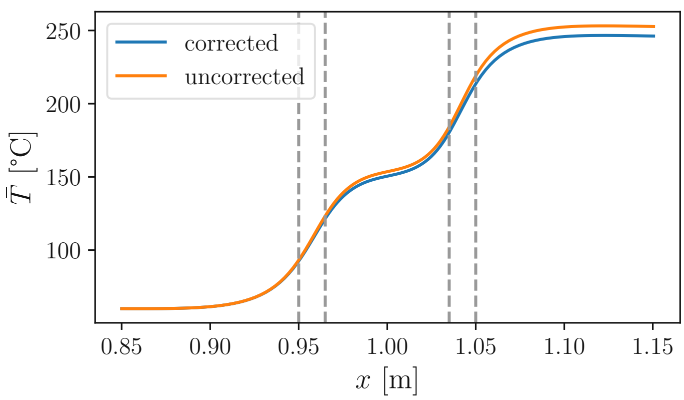

Figure 5.5: Comparison of the thickness-averaged temperatures in the slice. Dashed lines show the outline of the inductor arms.

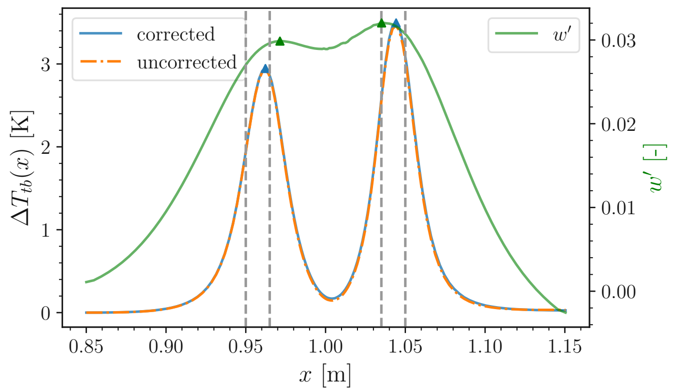

Figure 5.6: Comparison of temperature difference in the slice, for corrected $\Delta T_{c,tb}$ and uncorrected $\Delta T_{\mathrm{u,tb}}$ case. The right axis corresponds to the displacement derivative w'. Local maxima, $\hat{T}_{tb(1,2)}$ and $\hat{w}'_{(1,2)}$, are indicated by the ▲ markers. Dashed lines show the outline of the inductor arms.

leading to a lower temperature increase along the outer edge. The locally concentrated Joule losses lead to the temperature difference between top and bottom sheet, which occur only near the inductor, see Figure 5.4b. Because in addition to this temperature difference, deformations are present (see Figure 5.4d), this leads to a temperature error, see Figure 5.4c. The temperature error rises sharply under the first inductor arm, is transported downstream, rises under the second arm and is transported to the outflow boundary.

When inspecting the thickness-averaged temperature over the length of the cross-sectional slice, see Figure 5.5, it can also nicely be seen how the error increase is relatively local to the inductor arms. Moreover, because in this case the sign of the error forcing term f is always positive, there is a net-positive erroneous energy influx. Also, it may be pointed out that, the discrepancy between the corrected and uncorrected top and bottom temperature difference, $\Delta T_{c,tb}$ and $\Delta T_{\mathrm{u,tb}}$ are small in this setup, indicating almost fixed top and bottom temperatures–similar to a Dirichlet BC.

5.4 Comparison of Error Estimates

After having presented the results from the coupled FEM simulation, in the following, the error estimates obtained from the FEM simulation, the section model, and the numerically integrated error forcing are compared for the cross-section slice.

Discussion

The error comparison shows that integrating the forcing term yields a good approximation of the FEM error. Slight discrepancies might be due to the assumptions made in deriving the 1D model. For the error section method, it can be observed how the continuous increase is replaced by a discrete step, which however fits the (nearly) constant errors after each inductor. The slight undershoot for the first section was not alleviated by optimizing the factor C_1, because usually the section lengths Δx and maxima estimates of temperature and deflection are relatively uncertain anyway. It illustrates however that, if a practical formula for a section exists, here each inductor arm, then it may be used for all identical sections.

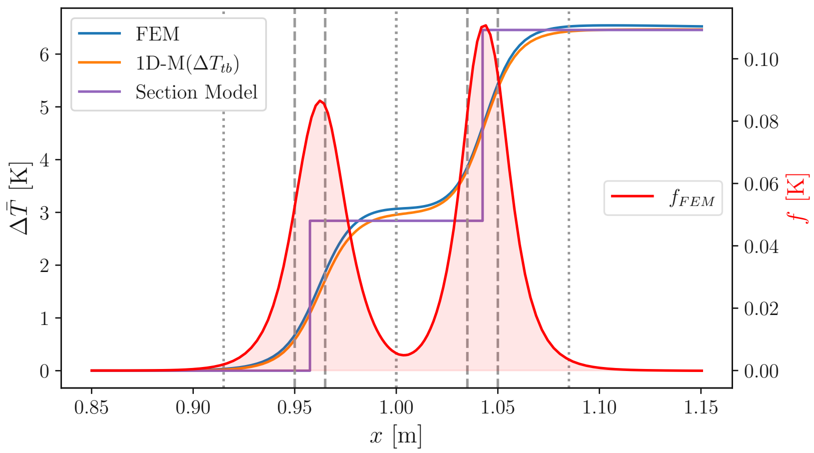

Figure 5.7: Comparison of errors and error forcing. The left axis corresponds to the errors from the FEM simulation, the section model, and the numerically integrated error forcing *1D-M*(ΔT_{tb}). The right axis corresponds to the error forcing $f_{FEM} = \Delta T_{\mathrm{tb}} w'$.

For a rough estimate of the error, if C is unknown and set to 1, would have given errors that are higher by a factor of 1.5. Of course, these are all statements about the thickness-averaged error. If the local error is important for a specific section, only the solution and comparison of both problems can give a definitive answer. Depending on how accurate the forcing term and length of a section are known, an appropriate uncertainty margin, say by using a factor of 5 to 10, may finally guide the decision for, or against, the addition of a velocity correction step.

6 Conclusion

This thesis has presented an investigation on the thermal behavior of revolving steel belts, with an emphasis on induction heating applications. By correcting the velocity field in the convection-diffusion equation with the Laplace equation, it was illustrated how deformations can be captured in a thermodynamically sound way. It was shown how the temperature fields differ in the corrected case compared with the uncorrected, and how an artificial energy in- or outflux results in a thickness-averaged temperature error. From this, a practical error estimation method was presented, where it was shown how the error is mainly arising in critical sections, where significant temperature differences between top and bottom surface occur.

In a parameter study for a 2D domain, errors where calculated for a range of speeds and deformation states. The assumptions for the simplified one-dimensional model were tested and an analytical estimate of the error was derived for this example. It was found that the inclusion of heat transfer effects can lead to an attenuation of the error, but that the maximum error is still well approximated by assuming no heat transfer for the error estimate.

To study the effects of deformation on the velocity related error in a more realistic scenario, a coupled electro-thermo-mechanical simulation was conducted. The results confirmed that, for an induction heating setup, zones of high Joule losses are critical. For the particular inductor setup, an ad-hoc method was presented to relate the section error with the inductor geometry and expected peak values for temperature difference and deformation. The resulting error approximations where found to be in good agreement with the simulation results. It was concluded, that in a less ideal setting, an appropriate error margin may be needed to accommodate for parameter uncertainties, but that the model captures the overall behavior.

Future work could explore alternative approaches for the thermo-mechanical problem, extending beyond the methods considered in this study. This work was limited to the steady-state case and focused on quasi-stationary belt deformations, leaving the investigation of transient behavior as an open avenue for further research. Given the relatively simple geometry of the belt, other computational methods, such as the finite-volume method (FVM), could also be explored as an alternative for solving the thermal problem, potentially offering different accuracy-efficiency trade-offs.

Furthermore, this study illustrated that temperature variations in the thickness direction are typically significant only in localized sections of the belt. Future research could focus on developing practical methods for adaptively discretizing the belt, allowing for more efficient numerical modeling. Building on the approach presented here – where sections with significant errors were approximated – semi-empirical equations could be leveraged to establish partial lumping criteria. This could facilitate a structured reduction from 3D to 2D/1D representations or even fully lumped sections, improving computational efficiency while maintaining accuracy.

Additionally, it would be valuable to investigate how established adaptive h-, p-, and hp-refinement methods, based on local error criteria, compare with such a partial lumping approach.

As mentioned in this work, accurately calculating heat transfer between the belt and surrounding air is challenging in general, and the interaction between the fluid and structure may be particularly interesting. Belt deformations may perturb the airflow, leading to localized variations in convective heat transfer, making a more detailed investigation of this interaction valuable. Future studies could incorporate computational fluid dynamics (CFD) simulations or coupled fluid-structure interaction (FSI) approaches to better capture these effects.

References

[1] T. L. Bergman, A. S. Lavine, F. P. Incropera, and D. P. DeWitt. *Fundamentals of Heat and Mass Transfer*. 8th edition. Wiley, 2017.

[2] A. N. Brooks and T. J. Hughes. “Streamline upwind/Petrov-Galerkin formulations for convection dominated flows with particular emphasis on the incompressible Navier-Stokes equations”. In: *Computer Methods in Applied Mechanics and Engineering* 32.1 (Sept. 1982), pp. 199–259.

[3] V. Filkin, Y. Vetyukov, B. Heinrich, and F. Toth. “Modelling the post-buckling behaviour of steel sheets under induction heating”. In: *PAMM* 23.2 (2023), e202300151.

[4] T. J. R. Hughes. *The finite element method : linear static and dynamic finite element analysis*. In collab. with Internet Archive. Mineola, NY : Dover Publications, 2000.

[5] M. Kaltenbacher. *Numerical Simulation of Mechatronic Sensors and Actuators: Finite Elements for Computational Multiphysics*. Berlin, Heidelberg: Springer Berlin Heidelberg, 2015.

[6] H. C. Kuhlmann. *Strömungsmechanik: eine kompakte Einführung für Physiker und Ingenieure*. 2., aktualisierte Aufl. Hallbergmoos: Pearson, 2014.

[7] K. Roppert, F. Toth, and M. Kaltenbacher. “Modeling Nonlinear Steady-State Induction Heating Processes”. In: *IEEE Transactions on Magnetics* 56.3 (Mar. 2020), pp. 1–4.

[8] K. Roppert. “Modelling and numerical simulation of induction heating processes for thin steel sheets”. Thesis. Technische Universität Wien, 2020.

[9] V. Simon, B. Weigand, and H. Gomaa. *Dimensional Analysis for Engineers*. Mathematical Engineering. Cham: Springer International Publishing, 2017.

[10] P. Stephan, S. Kabelac, M. Kind, D. Mewes, K. Schaber, and T. Wetzel, eds. *VDI-Wärmeatlas: Fachlicher Träger VDI-Gesellschaft Verfahrenstechnik und Chemieingenieurwesen*. Springer Reference Technik. Berlin, Heidelberg: Springer Berlin Heidelberg, 2019.

[11] Verein zur Förderung der Software openCFS. *OpenCFS*. 2025. URL: `https://opencfs.org/`.

[12] Y. Vetyukov. *Nonlinear Mechanics of Thin-Walled Structures: Asymptotics, Direct Approach and Numerical Analysis*. Foundations of Engineering Mechanics. Vienna: Springer Vienna, 2014.

[13] P. Wesseling. *Principles of Computational Fluid Dynamics*. Springer Science & Business Media, 2001.

[14] O. C. Zienkiewicz, R. L. Taylor, and P. Nithiarasu. *The finite element method for fluid dynamics*. Seventh edition. Oxford: Butterworth-Heinemann, 2014.

[15] O. C. Zienkiewicz, R. L. Taylor, and J. Z. Zhu. *The finite element method: its basis and fundamentals*. Seventh edition. Amsterdam: Elsevier, Butterworth-Heinemann, 2013.